Measurement 258 (2026) 119159

Contents lists available at ScienceDirect

Measurement

journal homepage: www.elsevier.com/locate/measurement

On the measurement of nonlinear aeroacoustics characteristics of solar cell structures using a novel metrological framework validated by a machine learning algorithm

Qiang Zhang [a], Lei Chang [b,*], Mohammed El-Meligy [c,d], Khalid A. Alnowibet [e]

[a] School of Environmental Science and Optoelectronic Technology, University of Science and Technology of China (USTC), Hefei, PR China
[b] School of Economics and Management, Anhui University of Science and Technology, Taifeng Road 168, Huainan 232001, Anhui Province, PR China
[c] Jadara University Research Center, Jadara University, PO Box 733, Irbid, Jordan
[d] Applied Science Research Center, Applied Science Private University, Amman, Jordan
[e] Department of Statistics and Operations Research, College of Science, King Saud University, Riyadh 11451, Saudi Arabia

ARTICLE INFO

Keywords:
Measurement
Nonlinear phase velocity
Lamb waves
Graphene platelets
Aeroacoustics
Solar cell structures

ABSTRACT

This study created a new metrological framework for the modeling of nonlinear phase velocity, propagation, and aeroacoustic evaluation of multilayer silicon solar cell structures with graphene platelet (GPL)-metal layers. The solar cells were evaluated under the combined external sound radiation effects and airflow pressure subjected to coupled vibrational acoustic responses. A corrected structural modeling method using higher-order shear deformation theory (HSDT), where transverse shear stresses continuously vary through the thickness, and modified couple stress theory (MCST) to account for size-dependent phenomena at the microscale. The governing partial differential equations using the variational energy method were constructed, and an analytical harmonic-based approach is used to solve the governing equations. The Newmark's transition is used to compute dynamic vibration response in order to accurately define transient outcomes. To ensure both reliability and predictive ability, the framework is validated with a hybrid deep neural network model (HDNNM) that uses machine learning to relate input parameters—GPL weight fraction, frequency stemmed from the excitation, and airflow velocity—to general nonlinear response performance metrics of sound pressure level and phase velocity changes. The contribution of the proposed mechanics-based modeling with machine learning represents a reliable method to evaluate metrics measured from metrology specific to solar cell structures subjected to aerodynamic acoustic conditions generally within the environmental regime. The findings further document the contributions of GPLs as strengthening or reinforcement of a structure's stiffness and damping characteristics, which similarly enhances a structure's energy conversion stability and acoustic properties. Lastly, these divergent thinking methodologies and experimental evidence will promote new insights into structural health monitoring, noise mitigation, and the evaluation of the next generation of solar energy devices.

1. Introduction

Plates and panels are fundamental structural elements in engineering, commonly used in the design of buildings, bridges, and aerospace structures [1]. They provide essential load-bearing capacity and contribute to the overall stability and safety of a system [2]. Engineers rely on plates and panels for their efficiency in distributing forces across a surface, making them ideal for applications like floors, walls, and roofs [3]. Their versatility also extends to advanced industries, such as automotive and aerospace, where lightweight and high-strength materials are crucial [4]. Understanding the behavior of these structures under different loads is vital for engineers to ensure performance, durability, and cost-effectiveness in their designs [5].

Photovoltaic (PV) devices are essential for engineers due to their role in harnessing renewable solar energy, which is crucial for reducing dependence on fossil fuels [6]. These devices convert sunlight into electricity, offering a sustainable and environmentally friendly solution to power generation [7]. Engineers must understand the efficiency and material science behind PV technology to optimize system designs for maximum energy output [8]. As the demand for clean energy solutions

* Corresponding author.
E-mail address: chang06@aust.edu.cn (L. Chang).

https://doi.org/10.1016/j.measurement.2025.119159
Received 4 April 2025; Received in revised form 14 September 2025; Accepted 26 September 2025
Available online 28 September 2025
0263-2241/© 2025 Elsevier Ltd. All rights are reserved, including those for text and data mining, AI training, and similar technologies.

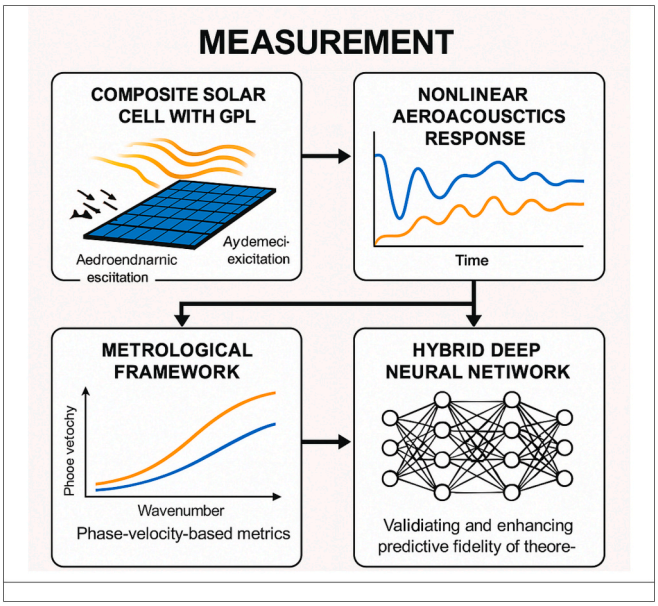

Fig. 1. A schematic view of the current problem using a novel metrological framework.

grows, integrating PV devices into buildings, infrastructure, and grids is becoming increasingly important [9]. Additionally, innovations in PV technology are pushing the boundaries of energy storage and off-grid applications, which are key to advancing sustainable engineering practices [10].

Graphene nanoplatelet reinforcement has become a game-changer in the field of materials engineering due to its exceptional mechanical, electrical, and thermal properties [11]. As a one-atom-thick layer of carbon atoms arranged in a hexagonal lattice, graphene is renowned for its unparalleled strength, being over 100 times stronger than steel while remaining incredibly lightweight [12]. Engineers have recognized the potential of graphene nanoplatelets as an additive to improve the strength, stiffness, and durability of various materials like composites, plastics, and metals [13]. The incorporation of GPLs into these materials can enhance their mechanical properties without significantly adding to their weight, making them ideal for industries such as aerospace, automotive, and construction [14]. Engineers are leveraging these properties to develop advanced cooling solutions for devices like smartphones, laptops, and electric vehicles, as well as for improving the performance of batteries and supercapacitors [15]. Moreover, the high surface area of graphene nanoplatelets allows for better bonding with other materials, which further improves the composite's performance [16]. Graphene's potential for enhancing the electrical conductivity of materials is also attracting significant attention from engineers working on next-generation sensors, wearable electronics, and flexible displays [17]. With GPLs integrated into polymer matrices, engineers can develop lightweight, flexible electronics that maintain high performance [18]. In the realm of energy storage, GPLs can be used to create more efficient and durable batteries and supercapacitors, offering faster charge times and longer lifespans [19]. The inclusion of graphene also promotes the development of energy-efficient coatings, where its strength and corrosion resistance ensure the longevity of structures exposed to harsh environments [20]. One of the major challenges engineers face with graphene nanoplatelet reinforcement is uniform dispersion within a material matrix, which is essential to fully realize its benefits [21]. Advanced processing techniques, like sonication and surface functionalization, are continually being developed to overcome this challenge [22]. Nonetheless, as research progresses, the integration of graphene nanoplatelets is becoming more viable, paving the way for next-generation materials with properties that far exceed those of traditional composites [23].

Wave propagation analysis is crucial for engineers as it helps predict how waves, such as sound, electromagnetic, or seismic waves, travel through different media [24]. This understanding is essential for designing structures that can withstand dynamic loads, such as vibrations, earthquakes, or acoustic pressures, ensuring their stability and safety [25]. In fields like civil engineering, wave propagation analysis aids in assessing soil-structure interactions and predicting how buildings and infrastructure will respond to ground motion during earthquakes [26]. In electrical engineering, it allows for the optimization of signal transmission in communication systems, ensuring data integrity and reducing interference [27]. Additionally, wave propagation plays a key role in material science, helping engineers understand how materials can be engineered to absorb, transmit, or reflect different types of waves for applications like shielding or energy harvesting [28]. In aerospace and automotive industries, it is critical to reduce noise and vibration in vehicles, improving comfort and performance [29]. Overall, wave propagation analysis provides engineers with the insights needed to design systems and structures that can effectively manage energy transfer and minimize unwanted impacts [30].

The measurement of dynamic and static stability is crucial for engineers to ensure the safety and functionality of structures and mechanical systems under various loading conditions [31]. Static stability assessment helps determine a system's ability to resist deformation or failure under constant or slowly varying loads [32]. In contrast, dynamic stability focuses on the system's response to time-dependent or sudden disturbances, such as vibrations, shocks, or aerodynamic forces [33]. Accurate measurement of both forms of stability enables engineers to predict critical thresholds, avoid instabilities like buckling or resonance, and design systems that maintain equilibrium under real-world conditions [34]. These measurements also guide material selection, structural optimization, and the development of advanced control strategies [35]. As engineering systems become more complex and lightweight, precise stability measurement becomes increasingly essential for innovation, safety, and long-term performance [36].

For the first time, a comprehensive metrological framework is introduced to assess the nonlinear phase velocity, Lamb wave propagation, and aeroacoustic characteristics of multi-layer silicon solar cell structures reinforced with GPL-metal layers. This framework accounts for the combined effects of sound radiation and airflow pressure on the dynamic behavior of solar cells, providing insights into vibro-acoustic interactions that influence performance. The model integrates HSDT, where shear stress is considered to vary with thickness, and the MCST to incorporate size-dependent effects. The underlying partial differential equations are resolved using a harmonic-based method and Newmark's time integration approach for transient dynamic analysis. To validate the results, an HDNNM is employed, combining machine learning algorithms with physical modeling to predict nonlinear responses under varying excitation frequencies, airflow velocities, and GPL weight fractions. This innovative methodology enables precise measurement of nonlinear acoustic responses and vibration characteristics, marking a significant advancement in the metrological analysis of solar cell structures. The study demonstrates the enhanced resilience of GPL-reinforced solar cells to dynamic loads, offering new opportunities for optimizing solar energy systems with improved noise control, energy efficiency, and structural health monitoring. A schematic view of the current problem using a novel metrological framework is shown in Fig. 1.

2. Mathematical modeling

As shown in Fig. 2, silicon solar cells are provided by this study. Glass

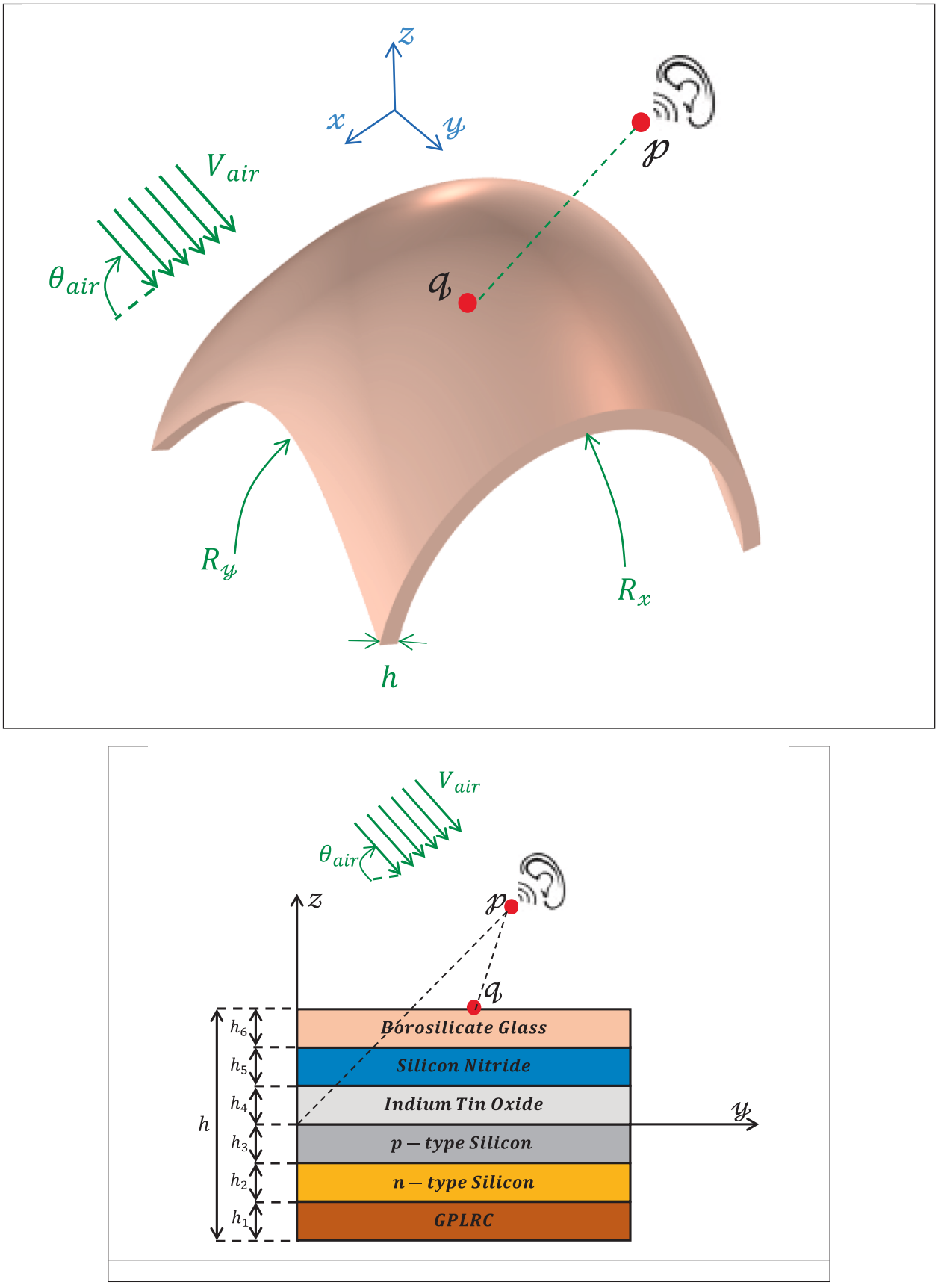

Fig. 2. A two-dimensional representation of a multi-layer silicon solar cell subjected to sound radiation and airflow pressure.

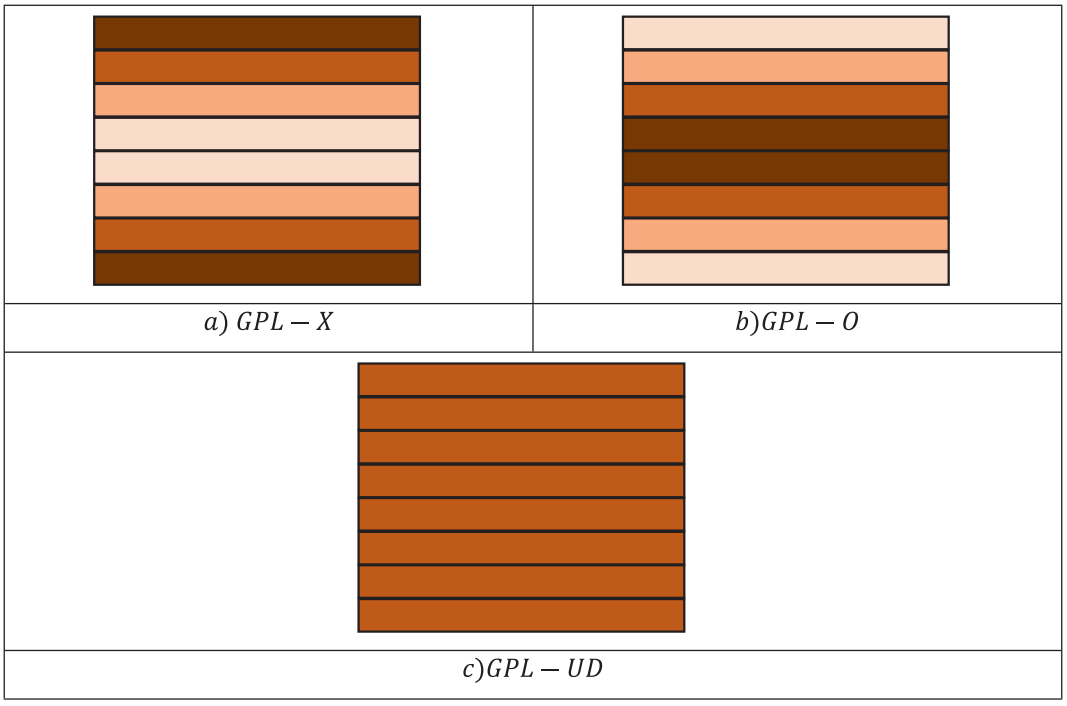

Fig. 3. Schematic of the various GPLRC.

Table 1
The silicon solar cell's material characteristics.

Layers	E (GPa)	ν	ρ (kg/m^3)	h (μm)	x
n-type Silicon	150	0.25	2300	0.01	$-\frac{h}{2}+h_1 < x < -h_3$
p-type Silicon	150	0.25	2300	0.01	$-h_3 < x < 0$
Indium Tin Oxide	70	0.35	6000	0.3	$0 < x < h_4$
Silicon Nitride	250	0.24	3440	0.1	$h_4 < x < h_4 + h_5$
Borosilicate Glass	69	0.23	2400	100	$h_4 + h_5 < x < \frac{h}{2}$

is the outermost of a solar cell's six layers, while the GPLRC reinforced metal layer is the innermost. A detailed depiction of the geometry and a three-dimensional schematic of this structure are provided in Fig. 2.

A thorough summary of each layer's material characteristics is provided in the results section, along with further geometric details.

2.1. Material properties

It should be noted that the classical isotropic relation $G=\frac{E}{2(1+\nu)}$ is not directly applicable to GPL-reinforced composites, because the incorporation of GPLs induces anisotropy. Therefore, instead of relying on isotropic assumptions, the effective elastic modulus of the GPLR nanocomposite is calculated using a modified version of the Halpin–Tsai model [37–40]. Three distinct distribution models that depict the dispersion of GPLs along the transverse direction are shown in Fig. 3. A modified version of the Halpin-Tsai equation [37–40] was used to calculate the GPLR nanocomposite's effective elastic modulus, yielding the following expression.

$$E_1(x)=-\frac{3}{8}\frac{1+\xi_L\eta_L V_{GPL}}{\eta_L V_{GPL}-1}\times E_m-\frac{5}{8}\frac{1+\xi_W\eta_W V_{GPL}}{\eta_W V_{GPL}-1}\times E_m. \quad -\frac{h}{2}<x<-\frac{h}{2}+h_1 \tag{1}$$

where $\xi_L=2\frac{l_{GPL}}{t_{GPL}}$, $\xi_W=2\frac{w_{GPL}}{t_{GPL}}$, $V^*_{GPL}=\frac{g_{GPL}}{\left(\frac{\rho_{GPL}}{\rho_m}\right)(1-g_{GPL})+g_{GPL}}$, $\eta_W=-\frac{1-\left(\frac{E_{GPL}}{E_m}\right)}{\xi_W+\left(\frac{E_{GPL}}{E_m}\right)}$, and $\eta_L=\frac{\left(\frac{E_{GPL}}{E_m}\right)-1}{\left(\frac{E_{GPL}}{E_m}\right)+\xi_L}$. Here, the orientation and aspect ratio of GPLs, represented by ξ_L and ξ_W introduce direction-dependent stiffness, which highlights the anisotropic nature of the GPLR nanocomposite. In addition to the effective modulus, the density and Poisson's ratio of the GPL-reinforced layer are obtained as weighted averages of the constituents, under the assumption of perfect interfacial bonding between GPLs and the metal matrix [41]:

$$\rho_1(x)=\rho_{GPL}V_{GPL}+\rho_m(1-V_{GPL}), \quad -\frac{h}{2}<x<-\frac{h}{2}+h_1 \tag{2}$$

$$\nu_1(x)=\nu_{GPL}V_{GPL}+\nu_m(1-V_{GPL}), \quad -\frac{h}{2}<x<-\frac{h}{2}+h_1$$

The volume content of GPL inside each of the previously mentioned GPL dispersion patterns (shown in Fig. 3) is represented mathematically in the text that follows:

$$\text{Pattern 1: GPL-X}: \quad V_{GPL}=4V^*_{GPL}\left|\frac{x+\frac{h}{2}-\frac{h_1}{2}}{h_1}\right| \quad -\frac{h}{2}<x<-\frac{h}{2}+h_1 \tag{3}$$

$$\text{Pattern 2: GPL-O}: \quad V_{GPL}=2V^*_{GPL}\left(1-2\left|\frac{x+\frac{h}{2}-\frac{h_1}{2}}{h_1}\right|\right) \quad -\frac{h}{2}<x<-\frac{h}{2}+h_1$$

Pattern 3: GPL-UD : $V_{GPL} = V^{*}_{GPL}$ $\quad -\frac{h}{2} < z < -\frac{h}{2}+h_1$

where $z = -\frac{h}{2} + \frac{(k-1)h_1}{N_L-1}$, $k = 1, \cdots, N_L$.These three dispersion patterns (GPL-X, GPL-O, and GPL-UD) are introduced to reflect the possible non-uniform distribution of GPLs along the thickness. The distribution significantly influences the effective elastic properties, as non-uniformity can either enhance or reduce the stiffness depending on the location of GPL-rich regions.

A number of GPL distribution patterns that show how material properties change with thickness direction are shown in Fig. 3.

Therefore, instead of applying simplified isotropic relations between E, ν, and ρ, the present model explicitly incorporates GPL dispersion patterns and interfacial bonding assumptions to capture the realistic effective properties of the GPLR nanocomposite layer.

A detailed presentation of GPL's material properties can be found in Ref. [42]. The material characteristics utilized in the construction of the contemporary cantilevered solar cell are listed in Table 1.

2.2. Theoretical formulation

Higher-order shear deformation theory can be used to define the displacement fields $u(x,y,z,t)$, $v(x,y,z,t)$, and $w(x,y,z,t)$ in order to derive a three-dimensional elasticity and apply it to a two-dimensional shell. According to this theory, shear stress changes with thickness. Therefore, if a system were already in place, there would be [43]:

$$u(x,y,z,t) = u_0(x,y,t) + zu_1(x,y,t) + z^2u_2(x,y,t) + z^3u_3(x,y,t)$$

$$v(x,y,z,t) = v_0(x,y,t) + zv_1(x,y,t) + z^2v_2(x,y,t) + z^3v_3(x,y,t)$$

$$w(x,y,z,t) = w_0(x,y,t)$$

The parameters for in-plane displacement are denoted by u_0, and v_0 in Eq. (4). Additionally, the displacement of a particular point (x,y) at the shell's midpoint is represented by w_0. Additionally, rotations around the y- and x-axes are represented by u_1 and v_1, respectively. In Taylor's series, higher-order terms are denoted as u_2, v_2, u_3, and v_3. One such expression for the structural strain–stress equation is Eq. (5) [44]:

$$\begin{bmatrix} \sigma_{xx} \\ \sigma_{yy} \\ \tau_{yz} \\ \tau_{xz} \\ \tau_{xy} \end{bmatrix} = \begin{bmatrix} \mathfrak{Q}_{11} & \mathfrak{Q}_{12} & 0 & 0 & 0 \\ \mathfrak{Q}_{21} & \mathfrak{Q}_{22} & 0 & 0 & 0 \\ 0 & 0 & \mathfrak{Q}_{44} & 0 & 0 \\ 0 & 0 & 0 & \mathfrak{Q}_{55} & 0 \\ 0 & 0 & 0 & 0 & \mathfrak{Q}_{66} \end{bmatrix} \begin{bmatrix} \varepsilon_{xx} \\ \varepsilon_{yy} \\ \gamma_{yz} \\ \gamma_{xz} \\ \gamma_{xy} \end{bmatrix}$$

$$\mathfrak{Q}_{11} = \mathfrak{Q}_{22} = \frac{E}{1-\nu^2},\ \mathfrak{Q}_{12} = \mathfrak{Q}_{21} = \frac{\nu E}{1-\nu^2}\ \mathfrak{Q}_{44} = \mathfrak{Q}_{55} = \mathfrak{Q}_{66} = \frac{E}{2(1+\nu)}. \tag{5}$$

We have:

$$E = \begin{cases} E_1 \ -\frac{h}{2} < z < -\frac{h}{2}+h_1 \\ E_2 \ -\frac{h}{2}+h_1 < z < -h_3 \\ E_3 \ -h_3 < z < 0 \\ E_4 0 < z < h_4 \\ E_5 h_4 < z < h_4 + h_5 \\ E_6 h_4 + h_5 < z < \frac{h}{2} \end{cases} \tag{6}$$

$$\nu = \begin{cases} \nu_1 \ -\frac{h}{2} < z < -\frac{h}{2}+h_1 \\ \nu_2 \ -\frac{h}{2}+h_1 < z < -h_3 \\ \nu_3 \ -h_3 < z < 0 \\ \nu_4 0 < z < h_4 \\ \nu_5 h_4 < z < h_4 + h_5 \\ \nu_6 h_4 + h_5 < z < \frac{h}{2} \end{cases}$$

$$\rho = \begin{cases} \rho_1 \ -\frac{h}{2} < z < -\frac{h}{2}+h_1 \\ \rho_2 \ -\frac{h}{2}+h_1 < z < -h_3 \\ \rho_3 \ -h_3 < z < 0 \\ \rho_4 0 < z < h_4 \\ \rho_5 h_4 < z < h_4 + h_5 \\ \rho_6 h_4 + h_5 < z < \frac{h}{2} \end{cases}$$

$\mathfrak{Q}_{ij}$ are the elastic coefficients related to the x, y, and z axes, whereas (σ_{xx}, σ_{yy}, τ_{yz}, τ_{xz}, τ_{xy}) indicate linear strain and (ε_{xx}, ε_{yy}, γ_{yz}, γ_{xz}, γ_{xy}) represent stresses. Accordingly, the strain–displacement correlations could be expressed as follows [45]:

$$\varepsilon_{xx} = \frac{\partial u}{\partial x} + \frac{w}{R_x} + \frac{1}{2}\left(\frac{\partial w}{\partial x}\right)^2,\ \varepsilon_{yy} = \frac{\partial v}{\partial y} + \frac{w}{R_y} + \frac{1}{2}\left(\frac{\partial w}{\partial y}\right)^2, \gamma_{xz} = \frac{\partial w}{\partial x} - \frac{u}{R_x} + \frac{\partial u}{\partial z}, \gamma_{yz} = \frac{\partial v}{\partial z} + \frac{\partial w}{\partial y} - \frac{v}{R_y},\ \gamma_{xy} = \frac{\partial v}{\partial x} + \frac{\partial u}{\partial y} + \frac{\partial w}{\partial x}\frac{\partial w}{\partial y} \tag{7}$$

The variational energy technique may be used to express the current system's motion equations and related boundary conditions [46,47]

$$\int_{t_1}^{t_2} (\delta\mathscr{T} - \delta\mathscr{U} - (\delta V_1 + \delta V_2))dt = 0$$

where the kinetic energy is [45]:

$$\delta\mathscr{T} = \iiint_V \rho\left(\frac{\partial u}{\partial t}\frac{\partial \delta u}{\partial t} + \frac{\partial v}{\partial t}\frac{\partial \delta v}{\partial t} + \frac{\partial w}{\partial t}\frac{\partial \delta w}{\partial t}\right)dV$$

When airflow pressure loading causes a change in work, δV can be written as follows:

$$\delta V_1 = -\int_A q_z \frac{\partial^2 w}{\partial x^2}\delta w dA \tag{10}$$

In which:

$$q_z = \frac{1}{2}\rho_{air}V_{air}^2\sin(\theta_{air}) \tag{11}$$

In this case, ρ_{air} indicates the air density, which is taken to be $\rho_{air} = 1.235\left[\mathrm{kg/m^3}\right]$ [48], while θ_{air} and V_{air} stand for the wind attack angle and average wind speed, respectively.

Additionally, the work performed by a transverse load that is harmonically excited can be written as

$$\delta V_2 = -\int_A q_0 \sin(\omega_{ext} t)\delta w dA \tag{12}$$

In this case, q_0 denotes the transverse load amount, and ω_{ext} denotes the excitation frequency. Furthermore, the following formula is used to determine the strain energy [45] associated with the current system, considering the modified couple stress theory.

$$\delta \mathscr{U} = \int_{-h/2}^{h/2}\iint_A \Big(\tau_{xy}\delta\gamma_{xy} + \sigma_{xx}\delta\varepsilon_{xx} + \sigma_{yy}\delta\varepsilon_{yy} + \tau_{xz}\delta\gamma_{xz} + \tau_{yz}\delta\gamma_{yz} + m^s_{xx}\chi^s_{xx} + m^s_{yy}\chi^s_{yy} + m^s_{zz}\chi^s_{zz} + m^s_{yz}\chi^s_{yz} + m^s_{xz}\chi^s_{xz} + m^s_{xy}\chi^s_{xy}\Big)\mathrm{dV}$$

Besides, χ^s_{ij}, and m^s_{ij} w hich can be defined as:

$$\chi^s_{ij} = \frac{1}{2}(\varphi_{i,j} + \varphi_{j,i}) \tag{14}$$

$$m^s_{ij} = 2l^2\mu\chi^s_{ij}$$

Also have:

$$\varphi = \frac{1}{2}\begin{bmatrix} i & j & k \\ \frac{\partial}{\partial x} & \frac{\partial}{\partial y} & \frac{\partial}{\partial z} \\ u & v & w \end{bmatrix} \tag{15}$$

v here

$$\varphi_x = \frac{1}{2}\left(\frac{\partial w_0}{\partial y} - v_1 - 2z v_2 - 3z^2 v_3\right) \tag{16}$$

$$\varphi_y = \frac{1}{2}\left(u_1 + 2z u_2 + 3z^2 u_3 - \frac{\partial w_0}{\partial x}\right)$$

$$\varphi_z = \frac{1}{2}\begin{pmatrix} \frac{\partial v_0}{\partial x} + z\frac{\partial v_1}{\partial x} + z^2\frac{\partial v_2}{\partial x} + z^3\frac{\partial v_3}{\partial x} \\ -\frac{\partial u_0}{\partial y} - z\frac{\partial u_1}{\partial y} - z^2\frac{\partial u_2}{\partial y} - z^3\frac{\partial u_3}{\partial y} \end{pmatrix}$$

Using the equations previously stated in Eq. (14) we obtain:

$$\chi_{xx} = \frac{\partial\varphi_x}{\partial x} = \left(\frac{\partial^2 w_0}{\partial x\partial y} - \frac{\partial v_1}{\partial x} - 2z\frac{\partial v_2}{\partial x} - 3z^2\frac{\partial v_3}{\partial x}\right) \tag{17}$$

$$\chi_{yy} = \frac{\partial\varphi_y}{\partial y} = \left(\frac{\partial u_1}{\partial y} + 2z\frac{\partial u_2}{\partial y} + 3z^2\frac{\partial u_3}{\partial y} - \frac{\partial^2 w_0}{\partial x\partial y}\right)$$

$$\chi_{zz} = \frac{\partial\varphi_z}{\partial z} = \begin{pmatrix} \frac{\partial v_1}{\partial x} + 2z\frac{\partial v_2}{\partial x} + 3z^2\frac{\partial v_3}{\partial x} \\ -\frac{\partial u_1}{\partial y} - 2z\frac{\partial u_2}{\partial y} - 3z^2\frac{\partial u_3}{\partial y} \end{pmatrix}$$

$$2\chi_{yz} = \frac{\partial\varphi_y}{\partial z} + \frac{\partial\varphi_z}{\partial y} = (2u_2 + 6zu_3) + \begin{pmatrix} \frac{\partial^2 v_0}{\partial x\partial y} + z\frac{\partial^2 v_1}{\partial x\partial y} + z^2\frac{\partial^2 v_2}{\partial x\partial y} + z^3\frac{\partial^2 v_3}{\partial x\partial y} \\ -\frac{\partial^2 u_0}{\partial y^2} - z\frac{\partial^2 u_1}{\partial y^2} - z^2\frac{\partial^2 u_2}{\partial y^2} - z^3\frac{\partial^2 u_3}{\partial y^2} \end{pmatrix}$$

$$2\chi_{xz} = \frac{\partial\varphi_x}{\partial z} + \frac{\partial\varphi_z}{\partial x} = (-2v_2 - 6zv_3) + \begin{pmatrix} \frac{\partial^2 v_0}{\partial x^2} + z\frac{\partial^2 v_1}{\partial x^2} + z^2\frac{\partial^2 v_2}{\partial x^2} + z^3\frac{\partial^2 v_3}{\partial x^2} \\ -\frac{\partial^2 u_0}{\partial x\partial y} - z\frac{\partial^2 u_1}{\partial x\partial y} - z^2\frac{\partial^2 u_2}{\partial x\partial y} - z^3\frac{\partial^2 u_3}{\partial x\partial y} \end{pmatrix}$$

$$2\chi_{xy} = \frac{\partial\varphi_x}{\partial y} + \frac{\partial\varphi_y}{\partial x} = \left(\frac{\partial^2 w_0}{\partial y^2} - \frac{\partial v_1}{\partial y} - 2z\frac{\partial v_2}{\partial y} - 3z^2\frac{\partial v_3}{\partial y}\right) + \left(\frac{\partial u_1}{\partial x} + 2z\frac{\partial u_2}{\partial x} + 3z^2\frac{\partial u_3}{\partial x} - \frac{\partial^2 w_0}{\partial x^2}\right)$$

Finally, the motion equations of the current system are obtained as follows by incorporating Eqs. (9), (10), (12), and (13) into Eq. (8):

$$\delta u_0 : \frac{\partial n_{xx}}{\partial x} + \frac{\partial n_{xy}}{\partial y} + \frac{n_{xz}}{R_x} + \frac{1}{2}\frac{\partial^2 n^{(0)}_{yz}}{\partial y^2} + \frac{1}{2}\frac{\partial^2 n^{(0)}_{xz}}{\partial x\partial y} = \imath_0\frac{\partial^2 u_0}{\partial t^2} + \imath_1\frac{\partial^2 u_1}{\partial t^2} + \imath_2\frac{\partial^2 u_2}{\partial t^2} + \imath_3\frac{\partial^2 u_3}{\partial t^2}$$

$$\delta v_0 : \frac{\partial n_{yy}}{\partial y} + \frac{\partial n_{xy}}{\partial x} + \frac{n_{yz}}{R_y} - \frac{1}{2}\frac{\partial^2 n^{(0)}_{yz}}{\partial x\partial y} - \frac{1}{2}\frac{\partial^2 n^{(0)}_{xz}}{\partial x^2} = \imath_0\frac{\partial^2 v_0}{\partial t^2} + \imath_1\frac{\partial^2 v_1}{\partial t^2} + \imath_2\frac{\partial^2 v_2}{\partial t^2} + \imath_3\frac{\partial^2 v_3}{\partial t^2}$$

$$\delta w_0 : -\left(\frac{n_{xx}}{R_x} + \frac{n_{yy}}{R_y}\right) + \frac{\partial n_{xz}}{\partial x} + \frac{\partial n_{yz}}{\partial y} + \frac{\partial}{\partial x}\left(n_{xx}\frac{\partial w_0}{\partial x}\right) + \frac{\partial}{\partial y}\left(n_{yy}\frac{\partial w_0}{\partial y}\right) + \frac{\partial}{\partial x}\left(n_{xy}\frac{\partial w_0}{\partial y}\right) + \frac{\partial}{\partial y}\left(n_{xy}\frac{\partial w_0}{\partial x}\right) - \frac{\partial^2 n^{(0)}_{xx}}{\partial x\partial y} + \frac{\partial^2 n^{(0)}_{yy}}{\partial x\partial y} - \frac{1}{2}\frac{\partial^2 n^{(0)}_{xy}}{\partial y^2} + \frac{1}{2}\frac{\partial^2 n^{(0)}_{xy}}{\partial x^2} - q_z = \imath_0\frac{\partial^2 w_0}{\partial t^2}$$

$$\delta u_1 : \frac{\partial m_{xx}}{\partial x} + \frac{\partial m_{xy}}{\partial y} + \frac{m_{xz}}{R_x} - n_{xz} + \frac{\partial n^{(0)}_{yy}}{\partial y} - \frac{\partial n^{(0)}_{zz}}{\partial y} + \frac{1}{2}\frac{\partial^2 m^{(0)}_{yz}}{\partial y^2} + \frac{1}{2}\frac{\partial^2 m^{(0)}_{xz}}{\partial x\partial y} + \frac{1}{2}\frac{\partial n^{(0)}_{xy}}{\partial x} = \imath_1\frac{\partial^2 u_0}{\partial t^2} + \imath_2\frac{\partial^2 u_1}{\partial t^2} + \imath_3\frac{\partial^2 u_2}{\partial t^2} + \imath_4\frac{\partial^2 u_3}{\partial t^2}$$

$$\delta v_1 : \frac{\partial m_{yy}}{\partial y} + \frac{\partial m_{xy}}{\partial x} + \frac{m_{yz}}{R_y} - n_{yz} - \frac{\partial n^{(0)}_{xz}}{\partial x} + \frac{\partial n^{(0)}_{zz}}{\partial x} - \frac{1}{2}\frac{\partial^2 m^{(0)}_{yz}}{\partial x\partial y} - \frac{1}{2}\frac{\partial^2 m^{(0)}_{xz}}{\partial x^2} - \frac{1}{2}\frac{\partial n^{(0)}_{xy}}{\partial y} = \imath_1\frac{\partial^2 v_0}{\partial t^2} + \imath_2\frac{\partial^2 v_1}{\partial t^2} + \imath_3\frac{\partial^2 v_2}{\partial t^2} + \imath_4\frac{\partial^2 v_3}{\partial t^2}$$

$$\delta u_2 : \frac{\partial n_{xx}}{\partial x} + \frac{\partial n_{xy}}{\partial y} + \frac{n_{xz}}{R_x} - 2m_{xz} + 2\frac{\partial m^{(0)}_{yy}}{\partial y} - 2\frac{\partial m^{(0)}_{zz}}{\partial y} + \frac{1}{2}\frac{\partial^2 n^{(0)}_{yz}}{\partial y^2} + \frac{1}{2}\frac{\partial^2 n^{(0)}_{xz}}{\partial x\partial y} + \frac{\partial m^{(0)}_{xy}}{\partial x} - n^{(0)}_{yz} = \imath_2\frac{\partial^2 u_0}{\partial t^2} + \imath_3\frac{\partial^2 u_1}{\partial t^2} + \imath_4\frac{\partial^2 u_2}{\partial t^2} + \imath_5\frac{\partial^2 u_3}{\partial t^2}$$

$$\delta v_2 : \frac{\partial n_{yy}}{\partial y} + \frac{\partial n_{xy}}{\partial x} + \frac{n_{yz}}{R_y} - 2m_{yz} - 2\frac{\partial m^{(0)}_{xz}}{\partial x} + 2\frac{\partial m^{(0)}_{zz}}{\partial x} - \frac{1}{2}\frac{\partial^2 n^{(0)}_{yz}}{\partial x\partial y} - \frac{1}{2}\frac{\partial^2 n^{(0)}_{xz}}{\partial x^2} - \frac{\partial m^{(0)}_{xy}}{\partial y} + n^{(0)}_{xz} = \imath_2\frac{\partial^2 v_0}{\partial t^2} + \imath_3\frac{\partial^2 v_1}{\partial t^2} + \imath_4\frac{\partial^2 v_2}{\partial t^2} + \imath_5\frac{\partial^2 v_3}{\partial t^2}$$

$$\delta u_3 : \frac{\partial q_{xx}}{\partial x} + \frac{\partial q_{xy}}{\partial y} + \frac{q_{xz}}{R_x} - 3p_{xz} + 3\frac{\partial p^{(0)}_{yy}}{\partial y} - 3\frac{\partial p^{(0)}_{zz}}{\partial y} - 3m^{(0)}_{yz} + \frac{1}{2}\frac{\partial^2 q^{(0)}_{yz}}{\partial y^2} + \frac{1}{2}\frac{\partial^2 q^{(0)}_{xz}}{\partial x\partial y} + \frac{3}{2}\frac{\partial p^{(0)}_{xy}}{\partial x} = \imath_3\frac{\partial^2 u_0}{\partial t^2} + \imath_4\frac{\partial^2 u_1}{\partial t^2} + \imath_5\frac{\partial^2 u_2}{\partial t^2} + \imath_6\frac{\partial^2 u_3}{\partial t^2}$$

$$\delta v_3 : \frac{\partial q_{yy}}{\partial y} + \frac{\partial q_{xy}}{\partial x} + \frac{q_{yz}}{R_y} - 3p_{yz} - 3\frac{\partial p^{(0)}_{xz}}{\partial x} + 3\frac{\partial p^{(0)}_{zz}}{\partial x} + 3m^{(0)}_{xz} - \frac{1}{2}\frac{\partial^2 q^{(0)}_{yz}}{\partial x\partial y} - \frac{1}{2}\frac{\partial^2 q^{(0)}_{xz}}{\partial x^2} - \frac{3}{2}\frac{\partial p^{(0)}_{xy}}{\partial y} = \imath_3\frac{\partial^2 v_0}{\partial t^2} + \imath_4\frac{\partial^2 v_1}{\partial t^2} + \imath_5\frac{\partial^2 v_2}{\partial t^2} + \imath_6\frac{\partial^2 v_3}{\partial t^2} \tag{18}$$

In which:

$$\int_V dV = \iint_A \int_{-\frac{h}{2}}^{\frac{h}{2}} dz dA = \iint_A \int_{-\frac{h}{2}}^{-\frac{h}{2}+h_1} dz dA + \iint_A \int_{-\frac{h}{2}+h_1}^{-\frac{h}{2}+h_1+h_2} dz dA + \iint_A \int_{-h_3}^{0} dz dA + \iint_A \int_{0}^{h_4} dz dA + \iint_A \int_{h_4}^{h_4+h_5} dz dA + \iint_A \int_{h_4+h_5}^{\frac{h}{2}} dz dA$$

$$\{n_{xx}, m_{xx}, p_{xx}, q_{xx}\} = \int_V \{1, z, z^2, z^3\}\sigma_{xx} dV$$

$$\{n_{yy}, m_{yy}, p_{yy}, q_{yy}\} = \int_V \{1, z, z^2, z^3\}\sigma_{yy} dV$$

$$\{n_{xz}, m_{xz}, p_{xz}, q_{xz}\} = \int_V \{1, z, z^2, z^3\}\tau_{xz} dV$$

$$\{n_{yz}, m_{yz}, p_{yz}, q_{yz}\} = \int_V \{1, z, z^2, z^3\}\tau_{yz} dV$$

$$\{n_{xy}, m_{xy}, p_{xy}, q_{xy}\} = \int_V \{1, z, z^2, z^3\}\tau_{xy} dV$$

$$\left\{n_{ij}^{(0)}, m_{ij}^{(0)}, p_{ij}^{(0)}, q_{ij}^{(0)}\right\} = \int_V \{1, z, z^2, z^3\} m_{ij} dV i, j = x, y, z$$

$$\{I_0, I_1, I_2, I_3, I_4, I_5, I_6\} = \int_V \rho\{1, z, z^2, z^3, z^4, z^5, z^6\} dV \quad (19)$$

By substituting Eq. (19) in to Eq. (18) we will have:

$$(\mathcal{K}_{\mathbf{L}} + \mathcal{K}_{\mathbf{NL1}} + \mathcal{K}_{\mathbf{NL2}})\mathcal{U} + \mathcal{M}\ddot{\mathcal{U}} = \mathbf{F}(t) \quad (20)$$

$$\mathcal{U} = [u_0 v_0 w_0 u_1 v_1 u_2 v_2 w_3 v_3]^T$$

While $\mathcal{K}_{\mathbf{NL1}}$ and $\mathcal{K}_{\mathbf{NL2}}$ are known as the nonlinear elastic stiffness matrices, which depend linearly and quadratically on the displacement vector, respectively, $\mathcal{K}_{\mathbf{L}}$ is the linear elastic stiffness matrix, $\mathbf{F}(t)$ is the dynamic load matrix, and $\mathcal{M}$ is the inertia matrix in this equation.

3. Solution method

3.1. Nonlinear PV

This section presents a harmonic-based method for resolving the basic partial differential equations (PDEs) governing the dynamic behavior of the system. Accordingly, the displacement fields are assumed in harmonic form as

$$\{u_i(x, y, t), v_i(x, y, t), w_0(x, y, t)\} = \{u_i^*(x, y, t), v_i^*(x, y, t), w_0^*(x, y, t)\} e^{(K_x x\sqrt{-1} + K_y y\sqrt{-1})} sin(\omega t), \; i = 1, 2, 3 \quad (21)$$

By substituting Eq. (21) into Eq. (20) with $\mathbf{F}(t) = 0$, the nonlinear frequency and the associated mode shape are obtained. Finally, the nonlinear phase velocity (NPV) is given by

$$NPV = \frac{\omega}{K_x} \quad (22)$$

It should be emphasized that the harmonic solution method in Eq. (21) is based on the assumption of weak nonlinearity, where the response can be adequately represented by a single harmonic component. In strongly nonlinear regimes—such as high GPL volume fractions or high-frequency excitations—this approximation may introduce errors, as higher-order harmonics and nonlinear coupling effects become significant. In such cases, more accurate approaches, such as direct numerical integration or nonlinear finite element simulations, can be employed to validate the harmonic-based solution.

3.2. Acoustic response

The dynamic displacement response of the arch under a time-dependent load is assessed using Newmark's time integration method in order to solve the dynamic vibration issue. The steps are described as follows:

Algorithm: (START)

Step 1 Initial calculation
1.1 $\mathcal{K} = \mathcal{K}_L$;
1.2 $\ddot{\mathcal{U}}_0 = \mathcal{M}^{-1}(\mathbf{F}_0 - \mathcal{K}\mathcal{U}_0)$
1.3 Select time step Δt;
1.4 $a_0 = \frac{1}{\beta(\Delta t)^2}$, $a_1 = \frac{\gamma}{\beta\Delta t}$, $a_2 = \frac{1}{\beta\Delta t}$, $a_3 = \frac{1}{2\beta} - 1$, $a_4 = \frac{\gamma}{\beta} - 1$, $a_5 = \frac{\Delta t}{2}\left(\frac{\gamma}{\beta} - 2\right)$, $a_6 = \Delta t(1-\gamma)$, $a_7 = \gamma\Delta t$;
Step 2 Calculate results for each time step $ts = 1, 2, \cdots, t/\Delta t$
2.1 $\widehat{\mathcal{K}} = \mathcal{K} + \frac{1}{\beta(\Delta t)^2}\mathcal{M}$
2.2 $\widehat{\mathbf{F}}_{ts} = \mathbf{F}_{ts} + \mathcal{M}\left(a_0 \mathcal{U}_{ts-1} + a_2 \dot{\mathcal{U}}_{ts-1} + a_3 \ddot{\mathcal{U}}_{ts-1}\right)$;
2.3 $\mathcal{U}_{ts} = \widehat{\mathcal{K}}^{-1}\widehat{\mathbf{F}}_{ts}$
2.4 Update and save the displacement, velocity and acceleration as
$\ddot{\mathcal{U}}_{ts} = a_0(\mathcal{U}_{ts} - \mathcal{U}_{ts-1}) - a_2 \dot{\mathcal{U}}_{ts-1} - a_3 \ddot{\mathcal{U}}_{ts-1}$
$\dot{\mathcal{U}}_{ts} = \dot{\mathcal{U}}_{ts-1} + a_6 \ddot{\mathcal{U}}_{ts-1} + a_7 \ddot{\mathcal{U}}_{ts}$
Step 3 Submitting $\mathcal{U}_{ts}$ into $\mathcal{K}_{NL}(\mathcal{U}_{ts})$ and setting $\mathcal{K} = \mathcal{K}_L + \mathcal{K}_{NL}(\mathcal{U}_{ts})$, replacing ts by $ts+1$ and repeating steps 2.1–2.4 for the next step.
(END)

The constant average acceleration scheme, which is defined by $\gamma = 0.5$, and $\beta = 0.25$, is used for all numerical calculations within the Newmark time integration framework. The velocity response is incorporated into the Rayleigh integral, which is stated in Eq. (23) to compute the acoustic pressure on the sandwich panel at a specific observation point (g).

$$p_p = \frac{i\omega\rho_0}{2\pi}\int_\Omega \frac{v(x, y, t)e^{-ik|p-g|}}{|p-g|} d\Omega \quad (23)$$

where ρ_0: density of the acoustic medium, k: acoustic wave number.

Eq. (24) is used to calculate the sound pressure level (SPL) in decibels (dB) for the sandwich panels that are displayed.

$$SPL = 20Log_{10}\frac{p_p}{p_{ref}} \quad (24)$$

where $p_{ref} = 2.0 \times 10^{-5} Pa$.

3.3. Formulation of lamb waves mathematically in the given green structure

The wave equation in a plate with free boundaries can be solved using lamb waves. There are two varieties of Lamb waves:

1. Symmetric (S) modes − Particle displacement is symmetric with respect to the plate's mid-plane.
2. Antisymmetric (A) modes: the displacement of particles is anti-symmetric with respect to the plate's mid-plane.

3.3.1. Dispersion relations

Based on the boundary conditions (stress-free plate surfaces), the dispersion relations for Lamb waves are as follows:

Symmetric Modes (S):

$$\tan(\gamma h)\tan(\gamma' h) = \frac{-4K_x^2\gamma\gamma'}{\left(K_x^2 - \gamma^2\right)^2} \quad (25)$$

Antisymmetric Modes (A):

$$\tan(\gamma h)\tan(\nu h) = \frac{\left(K_x^2 - \gamma^2\right)^2}{-4k^2\gamma\nu} \tag{26a}$$

$$\gamma = \sqrt{\frac{\omega_{NL}^2}{c_L^2} - K_x^2}, \nu = \sqrt{\frac{\omega_{NL}^2}{c_T^2} - K_x^2} \tag{26b}$$

The link between frequency ω_{NL}, wavenumber K_x, and wave speed c is established by these transcendental equations.

3.3.2. Numerical implementation

To solve these equations numerically:

3.3.2.1. Input material properties.

- Longitudinal wave speed (c_L)
- Shear wave speed (c_T)
- Plate thickness (h)

3.3.2.2. Frequency-wavenumber relationship.

- Define a range of frequencies ω_{NL} and wavenumbers K_x.
- For each (ω_{NL}, K_x), compute γ and ν.

3.3.2.3. Symmetric and antisymmetric modes.

- Analyze the dispersion relations' left- and right-hand sides (LHS and RHS) for symmetric and antisymmetric modes.
- Calculate the residuals, or the LHS-to-RHS difference.
- Use numerical techniques (such as Newton-Raphson) to determine the solutions K_x for each ω_{NL}.

3.3.3. Output for Figures

- **Contour Plots**

In a frequency-wavenumber domain, represent $|\text{LHS} - \text{RHS}|$ (residuals) for symmetric and antisymmetric modes.

- **3D Surface Plots**

Show $log_{10}(|\text{LHS} - \text{RHS}|)$ or $|\text{LHS} - \text{RHS}\}|$ as functions of frequency and wavenumber.

4. Hybrid deep neural networks

In recent years, the application of deep learning techniques to model complex physical systems has gained significant attention. Among these techniques, Convolutional Neural Networks (CNNs) and Long Short-Term Memory (LSTM) networks have proven particularly effective in handling spatial and temporal data, respectively. When combined, as in the case of Convolutional LSTM (ConvLSTM) models, these methods can capture spatiotemporal dynamics with higher accuracy. In this study, a hybrid deep neural network model, termed HDNNM, is proposed, utilizing CNN, LSTM, and ConvLSTM architectures to effectively capture the vibrational characteristics of the presented green structure. This approach offers a powerful framework for analyzing the behavior of such presented green structure under various stimuli, leveraging the strengths of deep learning to address the intricacies of mechanical interactions at various conditions. Here's a breakdown of the advantages and disadvantages of the hybrid deep neural network model compared to other algorithms in the context of analyzing electrodynamic features of the presented green structure:

4.1. Advantages

4.1.1. Capturing complex spatiotemporal dynamics

The combination of CNN, LSTM, and ConvLSTM in HDNNM allows the model to effectively capture both spatial and temporal relationships. CNNs excel at handling spatial dependencies, while LSTMs are adept at learning long-term dependencies in temporal sequences. ConvLSTM unifies these abilities, making it particularly suited for spatiotemporal problems.

4.1.2. Improved accuracy

By leveraging hybrid architectures, HDNNM can provide more accurate predictions and better generalization capabilities for complex dynamic phenomena. This advantage stems from the model's ability to simultaneously consider both the geometric structure and dynamic behavior over time.

4.1.3. Adaptability to nonlinear phenomena

This hybrid approach can better handle nonlinearities in electromechanical interactions due to the diversity of architectures integrated into a single model. LSTM can manage dynamic variations over time, while CNN and ConvLSTM can detect patterns that are often missed by traditional algorithms.

4.1.4. Robustness in diverse conditions

HDNNM is more robust in scenarios involving variable boundary conditions, non-uniform geometries, and varying material properties, which are common in green structures. Its hybrid nature enables it to adapt more effectively to different types of data input.

4.2. Disadvantages

4.2.1. Higher computational complexity

The integration of CNNs, LSTMs, and ConvLSTMs increases the overall computational burden. Training such a hybrid model requires more computational resources (e.g., GPU/TPU) and a longer training time compared to simpler models like traditional neural networks or standalone CNNs or LSTMs.

4.2.2. Risk of overfitting

Due to the large number of parameters involved, there is an increased risk of overfitting, especially if the training dataset is not sufficiently large or diverse. Regularization techniques, such as dropout or data augmentation, become crucial to mitigate this issue.

4.2.3. Complex hyperparameter tuning

Optimizing the performance of a hybrid model like HDNNM requires careful tuning of a wide range of hyperparameters, including learning rates, the number of layers, and filter sizes for CNNs, as well as the number of units and memory cells for LSTMs. This makes the development process more time-consuming and expertise-dependent.

4.2.4. Difficult interpretability

Hybrid deep learning models often function as black boxes, making it difficult to interpret the inner workings of the algorithm. Compared to more traditional machine learning models, it is harder to derive explicit insights into the underlying physics of the system from the model's parameters.

4.2.5. Potential for data scarcity issues

While the hybrid model can be powerful, its performance heavily depends on the quality and quantity of the training data. For rare or

complex phenomena where extensive datasets may not be available, the model could struggle to perform effectively, potentially underperforming against simpler models that are less data-hungry.

In summary, the hybrid deep neural network model offers substantial advantages in terms of capturing complex spatiotemporal dynamics and providing accurate predictions. However, it also introduces challenges related to computational demands, potential overfitting, and interpretability.

To simulate the hybrid deep neural network consisting of CNN, LSTM, and ConvLSTM, we need to outline the mathematical operations involved in each component of the hybrid model.

- CNN (Convolutional Neural Network)

The CNN is primarily responsible for extracting spatial features from the input data, often represented as a grid (e.g., a 2D image or a 2D representation of dynamic fields).

- Convolution Operation

For an input tensor X of shape $H \times W \times C_{in}$, where H is the height, W is the width, and C_{in} is the number of input channels (e.g., spatial dimensions or frequency modes), the convolution operation with kernel K of size $k_H \times k_W \times C_{in} \times C_{out}$ (where C_{out} is the number of output channels) is:

$$Y(i,j,c) = \sum_{m=0}^{k_H-1} \sum_{n=0}^{k_W-1} \sum_{C^*=0}^{k_H-1} X(i+m, j+n, C^*).K(m,n,C^*,C) \tag{27}$$

where Y is the output feature map, and i,j index spatial positions. The kernel slides across the input tensor and performs element-wise multiplication followed by summation.

- Activation (e.g., ReLU)

After convolution, an activation function like ReLU is applied to introduce non-linearity:

$$ReLU(z) = \max(0, z) \tag{28}$$

- LSTM (Long Short-Term Memory Network)

LSTM is used to handle the temporal aspect of the data, capturing time-dependent patterns such as how the electrodynamic features evolve over time. The LSTM has a complex internal structure with memory cells and gates (input, forget, and output gates).

- LSTM Equations

For a time step t, the input vector x_t, and previous hidden state h_{t-1}, the LSTM computes the following:

- Forget Gate:

$$f_t = \sigma\big(W_f.[h_{t-1}, x_t] + b_f\big) \tag{29}$$

- Input Gate:

$$i_t = \sigma(W_i.[h_{t-1}, x_t] + b_i)$$

- Cell State Update:

$$C^* = tanh(W_c.[h_{t-1}, x_t] + b_c) \tag{31}$$

- Cell State:

$$C_t = f_t.[C_{t-1}] + i_t.C^*)$$

- Output Gate:

$$o_t = \sigma(W_o.[h_{t-1}, x_t] + b_o) \tag{33}$$

- Hidden State:

$$h_t = o_t.tanh(C_t) \tag{34}$$

Here, W_f, W_i, W_C, W_o are weight matrices, b_f, b_i, b_C, b_o are biases, and σ denotes the sigmoid activation function.

- ConvLSTM (Convolutional LSTM)

ConvLSTM is a variant of LSTM where the internal operations are replaced by convolutional operations to capture both spatial and temporal correlations.

4.3. ConvLSTM equations

Instead of using matrix multiplications, ConvLSTM performs convolutional operations inside its gates. For an input tensor X_t at time step t, the operations are as follows:

- Forget Gate:

$$f_t = \sigma\big(W_f * [H_{t-1}, X_t] + b_f\big) \tag{35}$$

- Input Gate:

$$i_t = \sigma(W_i * [H_{t-1}, X_t] + b_i) \tag{36}$$

- Cell State Update:

$$C^* = tanh(W_c * [H_{t-1}, X_t] + b_c) \tag{37}$$

- Cell State:

$$C_t = f_t * [C_{t-1}] + i_t.C^*) \tag{38}$$

- Output Gate:

$$o_t = \sigma(W_o * [H_{t-1}, X_t] + b_o) \tag{39}$$

- Hidden State:

$$H_t = o_t * tanh(C_t) \tag{40}$$

Here, * denotes the convolution operation instead of matrix multiplication.

Table 2
Comparison of present results for the circular frequencies (ω) with the results of Ref. [49–51] ($\nu = 0.3, E = 210[GPa], \rho = 7480\left[Kg/m^3\right], h = 0.01[m], K_x = K_y, R_x = R_y = \infty$).

Mode number	2	5	8	11	14	17	20	23
Present	126.95	792.67	2026.76	3824.15	6177.21	9077.90	12514.75	16475.13
Ref. [50]	128.46	802.28	2050.90	3869.44	6250.88	9186.18	12664.47	16673.20
Ref. [51]	128.27	801.71	2052.38	3880.28	6285.41	9267.77	12827.37	16964.19
Ref. [49]	128.26	800.97	2047.55	3863.09	6240.55	9170.85	12643.1	16644.5

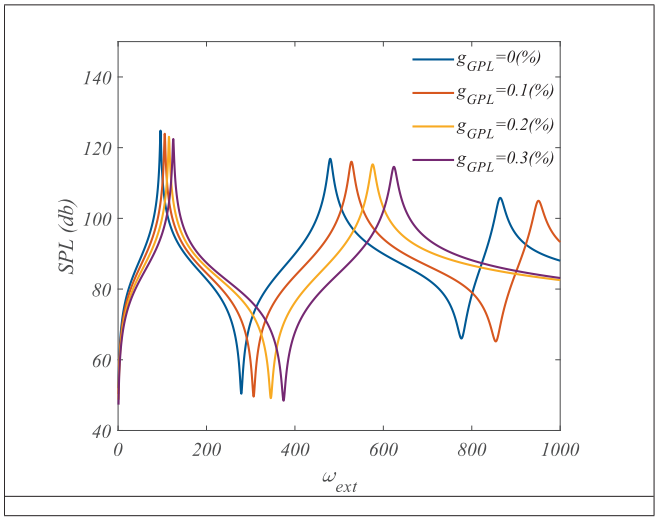

Fig. 4. The relationship between the sound pressure level and excitation frequency for solar cell structures with varying weight fractions of graphene platelet layers.

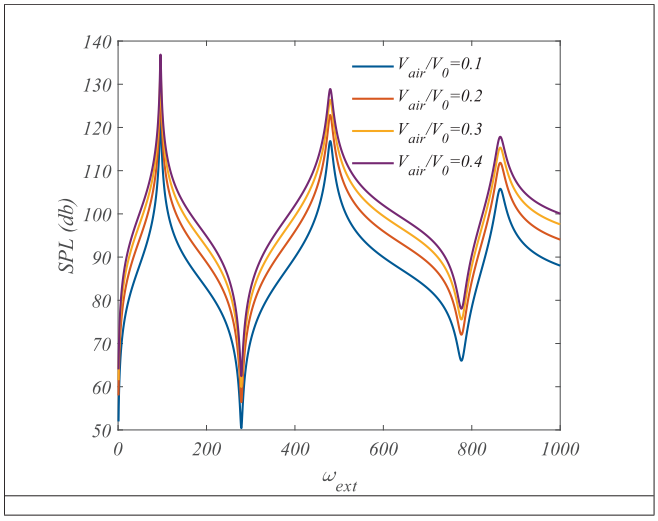

Fig. 5. The variation of sound pressure level with excitation frequency for different air flow velocities, expressed as a fraction of the reference velocity.

4.4. Hybrid model (HydroDL)

To simulate the hybrid algorithm, we combine these components in a sequential or parallel architecture. The workflow could be:

- Step 1: CNN for Spatial Feature Extraction

Apply the CNN layers to the input data X (e.g., spatial data representing the presented green structure).

- Step 2: LSTM for Temporal Dynamics

The output of the CNN is reshaped into a sequence and fed into LSTM layers to capture temporal dependencies.

- Step 3: ConvLSTM for Spatiotemporal Modeling

Alternatively, ConvLSTM can be used either before or after the LSTM to model both spatial and temporal correlations simultaneously, especially for data that exhibits strong spatial–temporal coupling.

5. Parametric results

5.1. Validation study

Table 2 presents a detailed comparison of the present study's results for circular frequencies (ω) with those from three referenced studies ([49–51]) under identical conditions, including a velocity (ν) of 0.3, Young's modulus (E) of 210 GPa, density (ρ) of 7480 kg/m^3, thickness of 0.01 m, and the same wave numbers for both directions ($K_x = K_y$). The frequencies are provided for various modes, from Mode 2 to Mode 23, allowing for a comprehensive evaluation of the present model's accuracy and consistency with previous work. The data in Table 2 shows minor discrepancies in the circular frequencies between the present results and the references. For instance, in Mode 2, the present frequency (126.95 MHz) is very close to the value from Ref. [50] (128.46 MHz) and Ref. [51] (128.27 MHz), indicating high consistency. Similarly, for higher modes (e.g., Mode 23), the frequencies calculated in the present study (16475.13 MHz) align closely with the referenced values. These comparisons emphasize the reliability and validation of the present study's results against established research, providing confidence in the robustness of the methodology and the accuracy of the computed frequencies across a broad range of modes. This comparison table serves as an important benchmark for verifying the present study's outcomes and ensuring the precision of the Lamb wave model in complex structural applications.

5.2. Parametric results

Fig. 4 presents the relationship between the sound pressure level (SPL) and excitation frequency (ω_{ext}) for solar cell structures with varying weight fractions of graphene platelet layers, ranging from 0 % to 0.3 %. The SPL is observed to exhibit a complex, nonlinear variation with frequency, characterized by several peaks and valleys. As the excitation frequency increases, the intensity of the SPL tends to rise for all GPL content values, with the highest SPLs corresponding to the greatest GPL weight fractions. Notably, the introduction of GPLs shifts the frequency response and amplifies the acoustic signals, particularly at higher frequencies, indicating an enhancement in the nonlinear aeroacoustic behavior of the system. The presence of GPLs, with their unique mechanical properties, likely contributes to the increased sound absorption or transmission within the solar cell structure, altering its resonance characteristics. The nonlinear behavior observed here can be attributed to the changes in material stiffness and damping as a result of incorporating GPLs. This highlights the significant role that material composition plays in modulating the aeroacoustic performance of solar

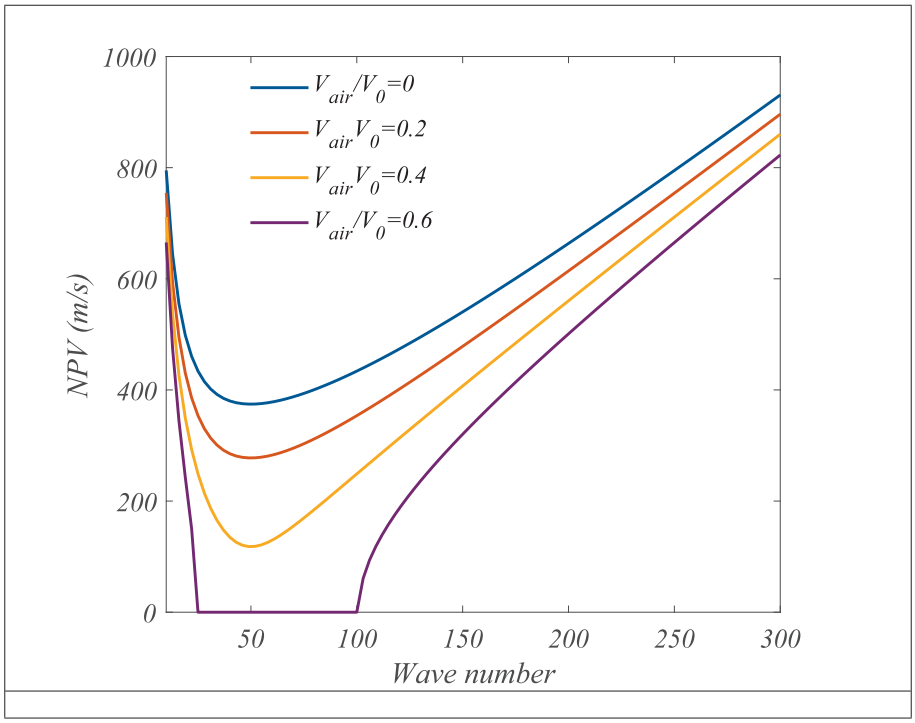

Fig. 6. The nonlinear phase velocity as a function of wave number for different air flow velocities, normalized by the reference velocity.

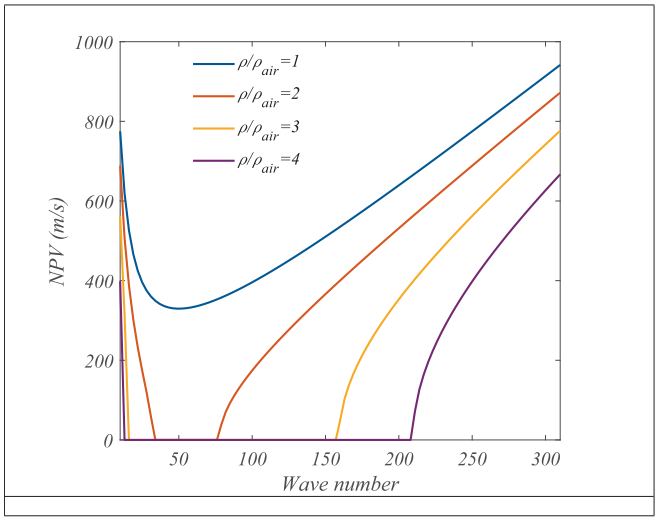

Fig. 7. The nonlinear phase as a function of wave number for different densities, normalized by the reference air density.

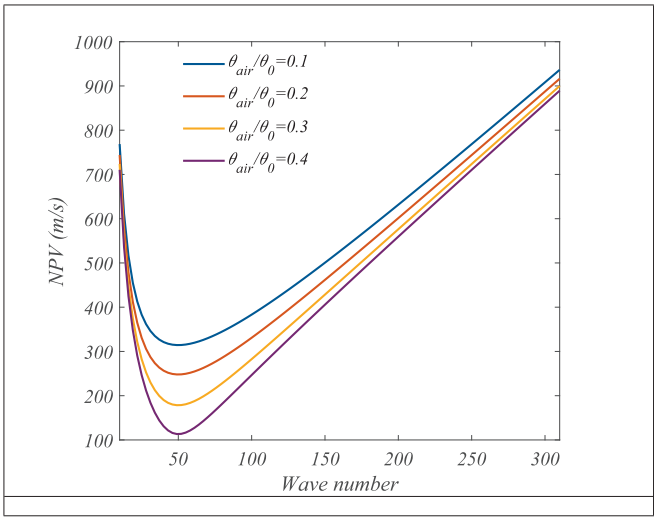

Fig. 8. The nonlinear phase velocity as a function of wave number for different airflow angles, normalized by the reference angle.

cells, especially in the presence of turbulent air flows and external excitations.

Fig. 5 shows the variation of sound pressure level with excitation frequency for different air flow velocities, expressed as a fraction of the reference velocity. The curves represent air flow velocities ranging from 0.1 V_0 to 0.4 V_0. As the air velocity increases, the SPL increases, demonstrating the enhanced acoustic response due to faster airflow. The frequency response exhibits complex nonlinear behavior, with pronounced peaks and dips at certain excitation frequencies. Higher air velocities result in sharper SPL variations, particularly at higher frequencies. The system's acoustic response is influenced by the interaction between turbulent air and the solar cell structure, which changes as the air flow velocity increases. Faster air velocities introduce more intense turbulence, which in turn affects the propagation of sound waves through the medium, likely increasing the overall sound energy and leading to stronger resonance effects. The nonlinearities observed in the SPL with increasing air velocity suggest that the flow-induced turbulence has a significant impact on the acoustic characteristics, particularly in the nonlinear regime. This behavior is critical for understanding how variable air velocities influence the aeroacoustic response in solar cell systems under different operational conditions.

Fig. 6 displays the nonlinear phase velocity as a function of wave number for different air flow velocities, normalized by the reference velocity. The curves show a distinct nonlinear relationship between NPV and wave number, with higher air flow velocities resulting in higher NPV values across all wave numbers. The NPV decreases as the wave number increases, indicating the typical behavior of wave propagation through a nonlinear medium, where higher frequencies experience

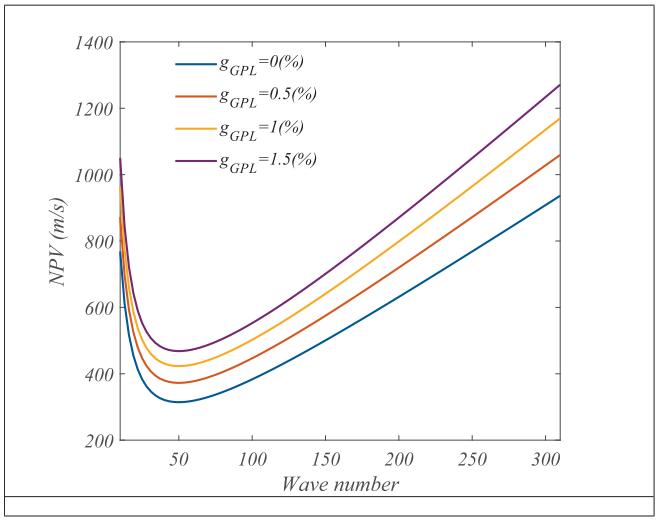

Fig. 9. The nonlinear phase velocity as a function of wave number for different graphene platelet layer weight fractions.

slower propagation speeds. At lower air flow velocities, the NPV is lower, reflecting the reduced energy in the system due to slower-moving air. As the air velocity increases, the NPV increases significantly, suggesting that faster air flow accelerates wave propagation by imparting more energy to the acoustic waves. The variation in NPV with wave number further highlights the complex interaction between the turbulent air flow and the solar cell structure. These interactions lead to the modification of the wave properties, particularly in the nonlinear regime, where the phase velocity is no longer constant but varies with both wave number and air velocity. The nonlinear response in this context plays a critical role in understanding how acoustic waves behave in systems subjected to varying airflow conditions.

In Fig. 7, the nonlinear phase velocity is shown as a function of wave number for different densities, normalized by the reference air density. The figure demonstrates that higher densities lead to higher NPV values across all wave numbers, particularly at lower wave numbers. As density increases, the propagation of acoustic waves is slower at lower frequencies, but this effect diminishes as the wave number increases. This behavior suggests that denser increases the inertia of the medium, resulting in slower acoustic wave propagation, particularly at low frequencies. At higher wave numbers (or higher frequencies), the effect of density on NPV becomes less pronounced, and the phase velocity increases. The nonlinear phase velocity is influenced by the density, and the system exhibits stronger nonlinearities as the density increases. This behavior indicates that changes in density, either due to environmental conditions or design modifications, significantly affect the acoustic properties of the solar cell system. By controlling the density, the acoustic performance of the system could be tailored, which is crucial for optimizing the nonlinear aeroacoustic characteristics of solar cells under different operational scenarios.

Fig. 8 presents the nonlinear phase velocity as a function of wave number for different airflow angles, normalized by the reference angle. The curves represent varying airflow angles, ranging from 0.1 to 0.4 of the reference value. As air density increases, the NPV decreases at lower wave numbers, reflecting the denser medium's impact on acoustic wave propagation. Higher airflow angles result in a slower propagation of waves at lower frequencies due to increased inertia in the medium. At higher wave numbers (or frequencies), the NPV begins to converge across different airflow angles, indicating that the effect of airflow angle on wave speed diminishes at high frequencies. This behavior demonstrates the nonlinear relationship between airflow angle and acoustic wave propagation, where increased density leads to significant reductions in phase velocity at lower frequencies, but this effect becomes

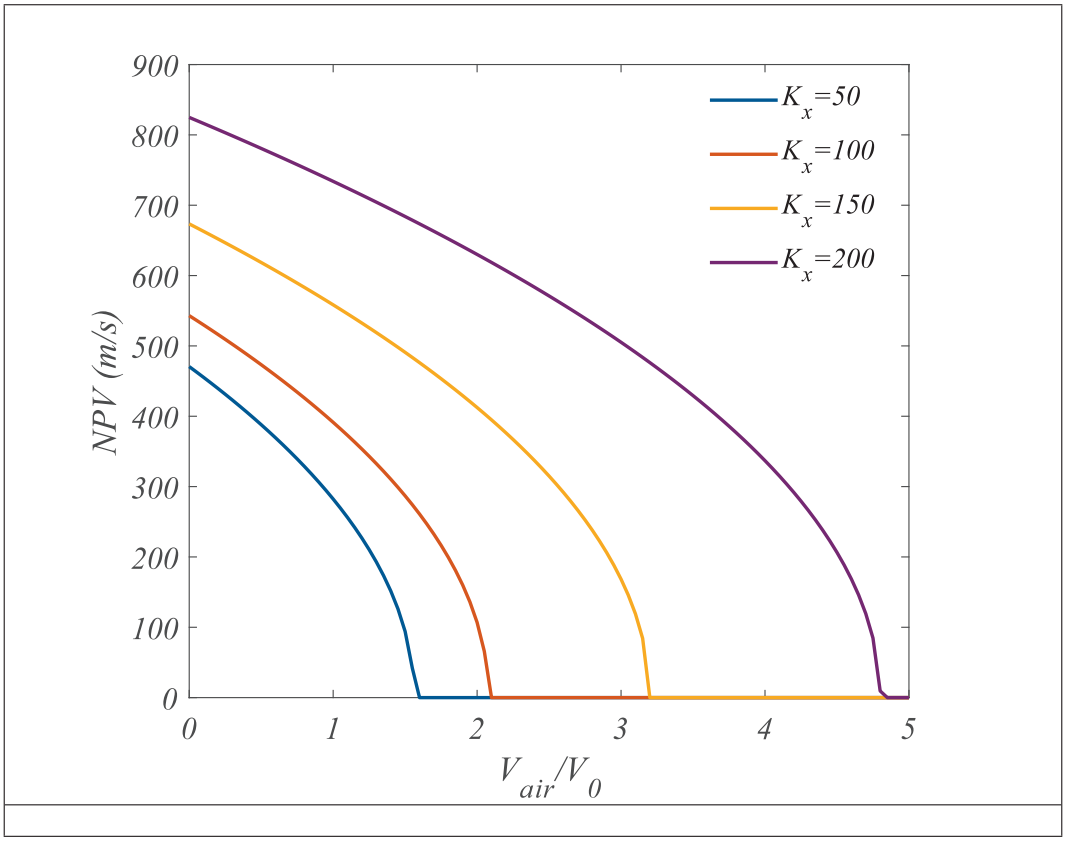

Fig. 10. The nonlinear phase velocity against the airflow velocity for different wave numbers.

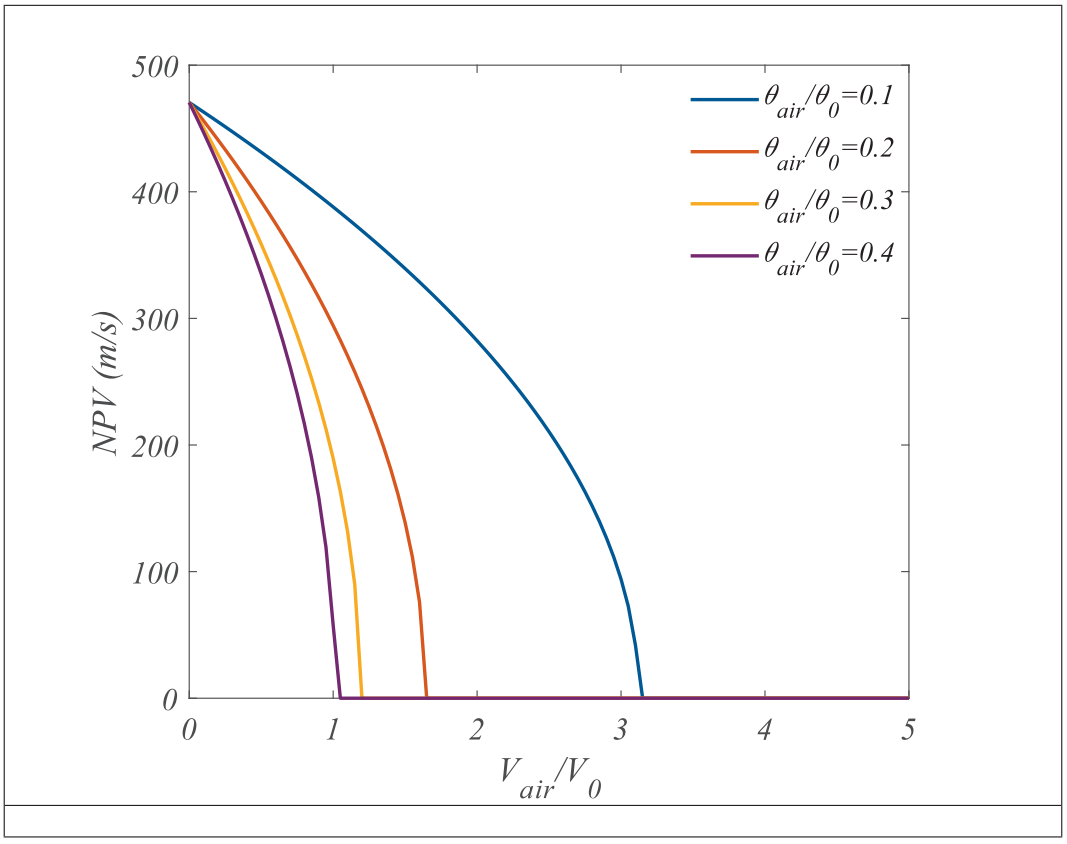

Fig. 11. The nonlinear phase velocity as a function of airflow velocity for varying airflow angle ratios.

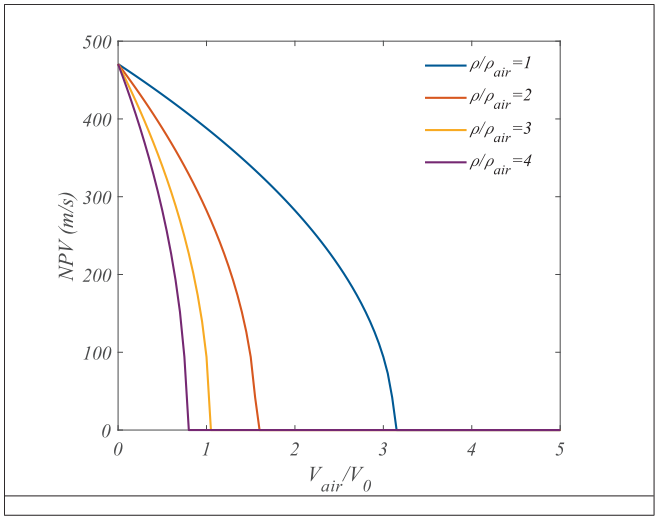

Fig. 12. The nonlinear phase velocity as a function of airflow velocity for varying densities.

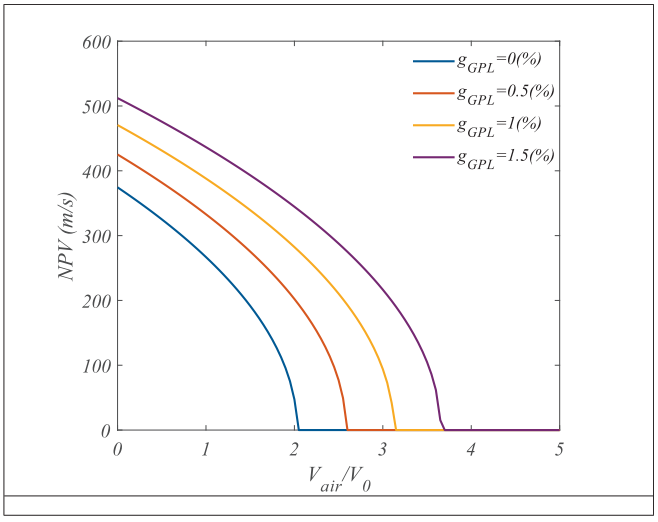

Fig. 13. The nonlinear phase velocity as a function of airflow velocity for varying graphene platelet layer weight fractions, ranging from 0% to 1.5%.

less pronounced at higher frequencies. The plot emphasizes the importance of airflow angle in influencing the nonlinear phase velocity, which in turn affects the overall acoustic performance and response of the system under varying environmental conditions.

Fig. 9 shows the nonlinear phase velocity as a function of wave number for different graphene platelet layer weight fractions, ranging from 0 % to 1.5 %. As the g_{GPL} increases, the NPV at a given wave number also increases. This trend suggests that the inclusion of GPLs in the material structure enhances the phase velocity of the acoustic waves. The presence of GPLs modifies the material properties, such as stiffness and damping, which directly influence the propagation speed of the waves. The curves show that higher GPL fractions lead to a marked increase in NPV, particularly noticeable at higher wave numbers (frequencies). This indicates that the material's ability to transmit sound waves is significantly enhanced with the incorporation of GPLs, resulting in faster wave propagation. The nonlinear response observed in this plot underscores the critical role of material composition in determining the aeroacoustic characteristics of solar cell structures, especially in

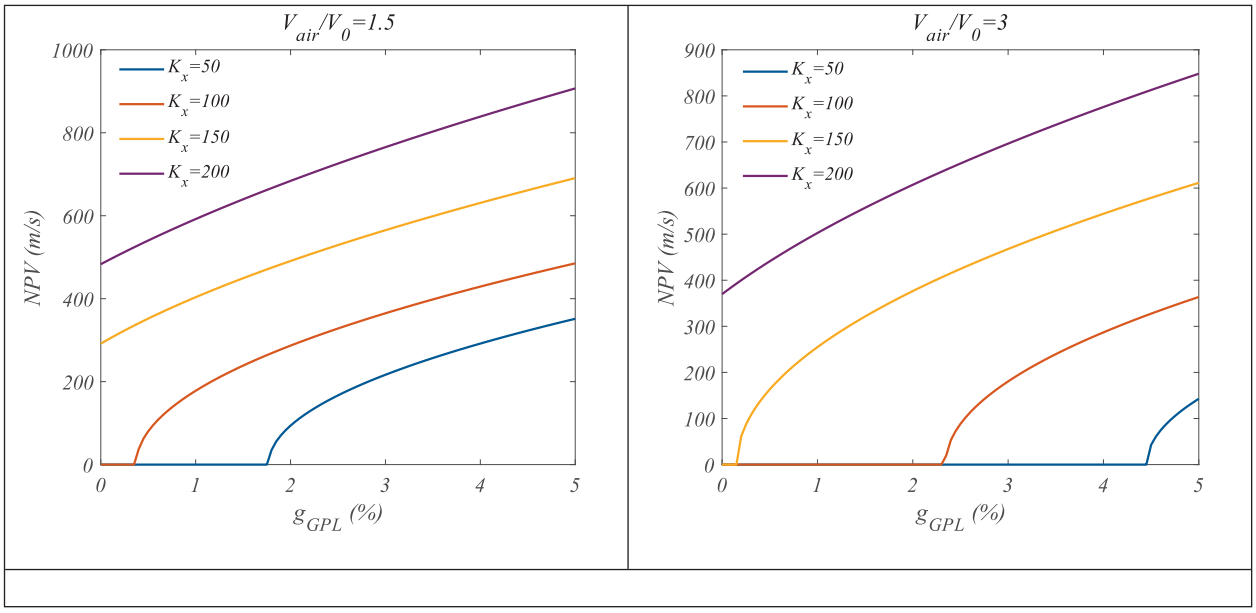

Fig. 14. The relationship between nonlinear phase velocity and the GPLs' weight fraction for different wave numbers at two different values of air velocity ratio.

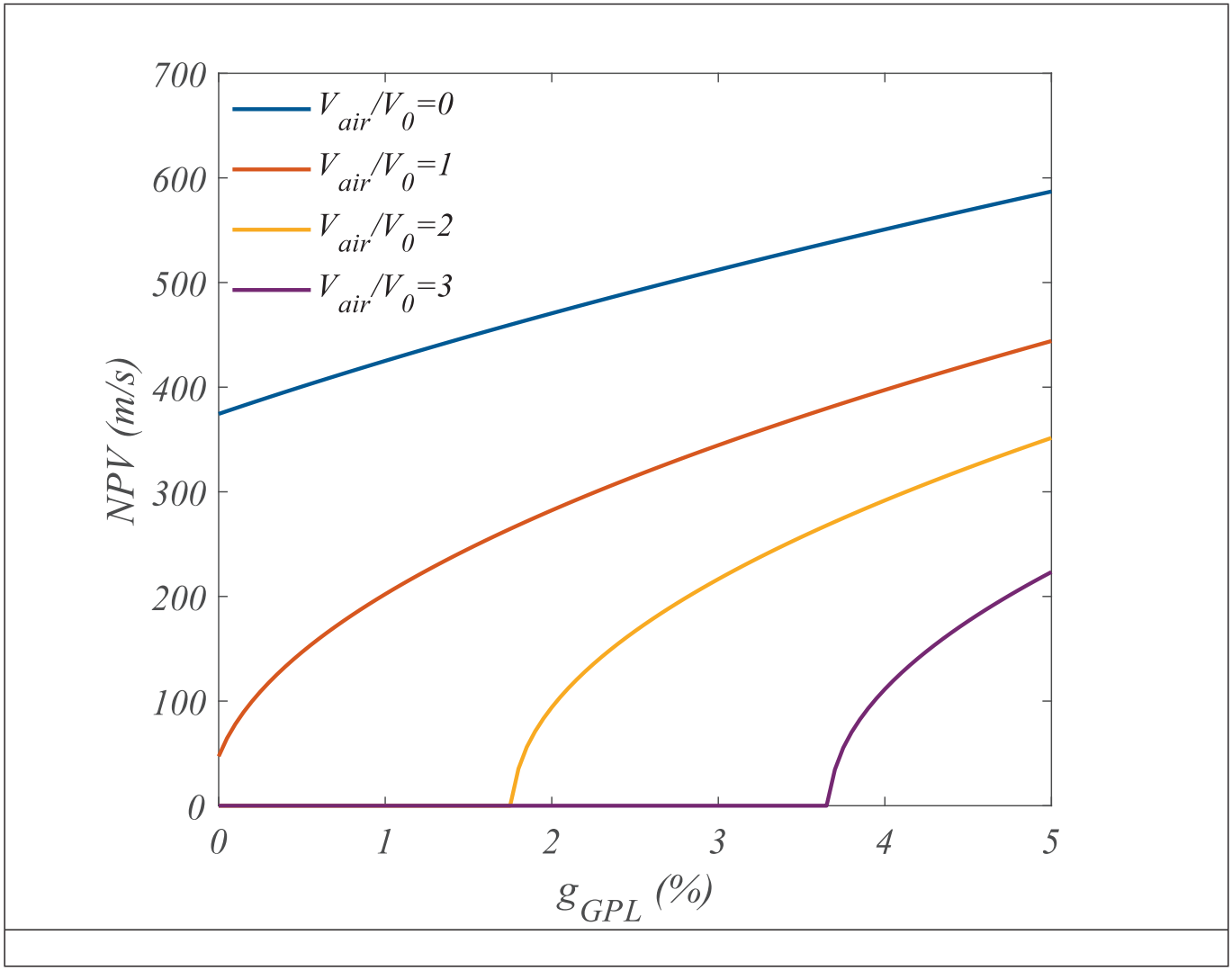

Fig. 15. The nonlinear phase velocity as a function of the GPL weight fraction for different airflow velocities.

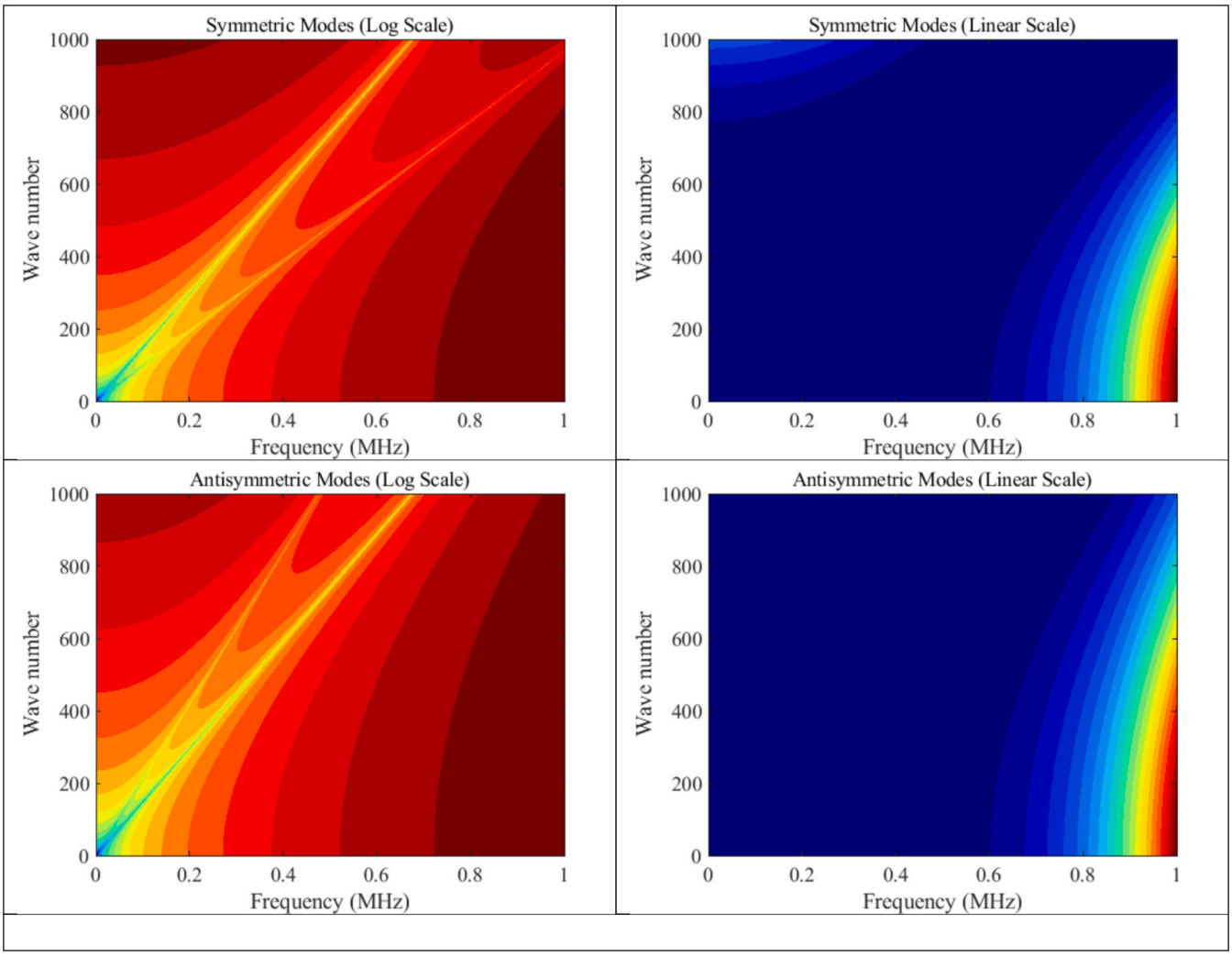

Fig. 16. The frequency-wave number dispersion plots for symmetric and antisymmetric modes of Lamb waves, in both logarithmic and linear scales, at a fixed GPL weight fraction.

high-frequency regimes where GPLs exert a pronounced influence on phase velocity.

In Fig. 10, the nonlinear phase velocity is plotted against the airflow velocity for different wave numbers. The curves represent wave numbers ranging from 50 to 200, and as the airflow velocity increases, the NPV decreases for each wave number. This inverse relationship indicates that faster air flow reduces the nonlinear phase velocity, possibly due to the increased energy dissipation in the system. Higher airflow velocities cause stronger turbulent interactions between the air and the structure, leading to more complex acoustic behavior. The curves for higher wave numbers exhibit sharper decreases in NPV as the airflow velocity increases, indicating that high-frequency waves are more susceptible to the effects of air velocity. This plot highlights how both the air velocity and wave number interact to influence the nonlinear phase velocity, underlining the importance of controlling these parameters to optimize the acoustic performance of solar cell structures in real-world conditions.

Fig. 11 illustrates the relationship between nonlinear phase velocity and the ratio of air velocity to reference velocity for various airflow angle ratios. The plot presents curves for four different airflow angle ratios: 0.1 (blue), 0.2 (red), 0.3 (yellow), and 0.4 (purple). As shown in the graph, for each airflow angle ratio, the NPV decreases significantly as the air velocity ratio increases. The curves exhibit a similar pattern, with a steep drop in NPV at lower air velocity ratios and a gradual leveling off as the ratio increases. This behavior suggests that the nonlinear phase velocity is highly sensitive to both the airflow angle ratio and the air velocity. For smaller airflow angle ratios (e.g., $\theta_{air}/\theta_0 = 0.1$), the NPV values remain relatively higher compared to larger ratios, indicating a greater influence of the airflow angle on the system's dynamic response. As the airflow angle ratio increases, the NPV values decrease more sharply, reflecting a reduction in the system's responsiveness to the varying air velocity. The results demonstrate the complex interaction between airflow characteristics and the structural dynamics, offering valuable insights into the impact of airflow directionality on nonlinear vibrational behavior.

Fig. 12 illustrates the nonlinear phase velocity as a function of airflow velocity for varying densities, normalized by the reference air density. The curves represent densities from 0.1 to 0.4 of the reference value, showing that as the density increases, the NPV decreases for a given airflow velocity. At higher densities, the wave propagation is slower for low airflow velocities, but the effect of density diminishes as the airflow velocity increases. This behavior reflects the interplay between density and velocity, where denser air leads to a more significant reduction in phase velocity at lower velocities, but faster air flows counteract the effect of density, leading to a less pronounced difference in NPV at higher velocities. The figure emphasizes the complex nonlinear nature of acoustic wave propagation in a medium where both density and airflow velocity must be considered to understand the overall behavior of sound waves in solar cell structures. This highlights the need for careful optimization of these parameters in practical

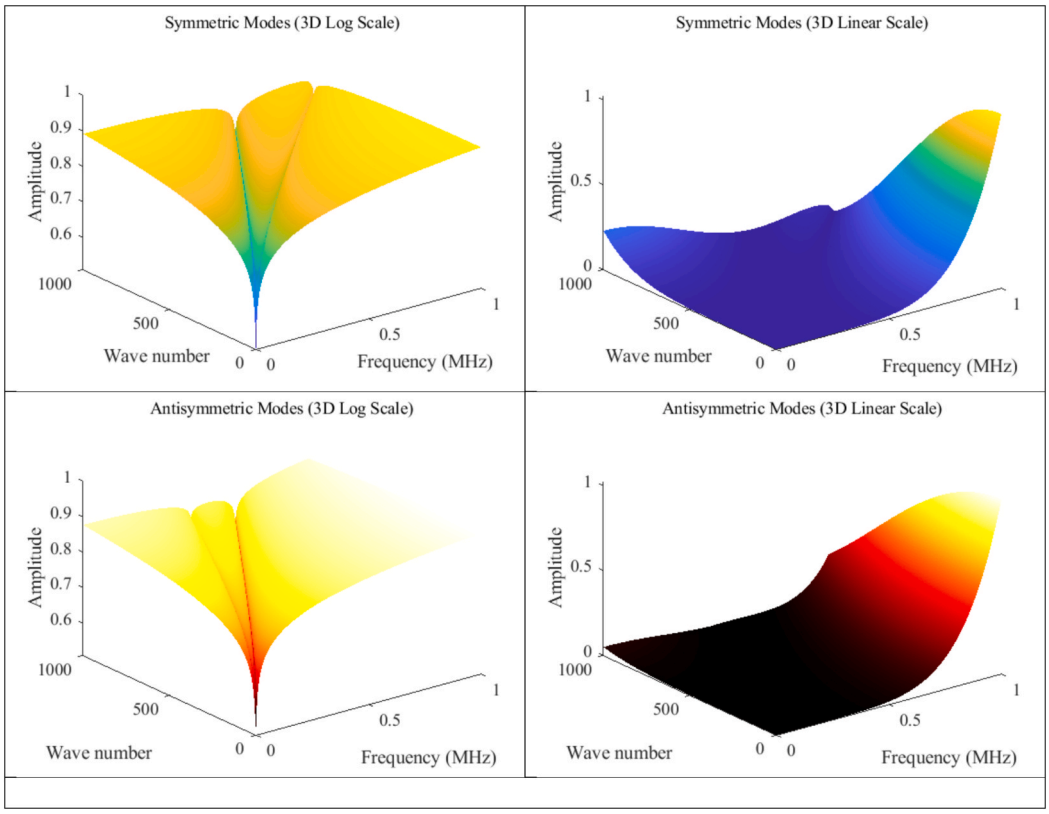

Fig. 17. The 3D dispersion plots for the symmetric and antisymmetric modes of Lamb waves, displayed in both logarithmic and linear scales.

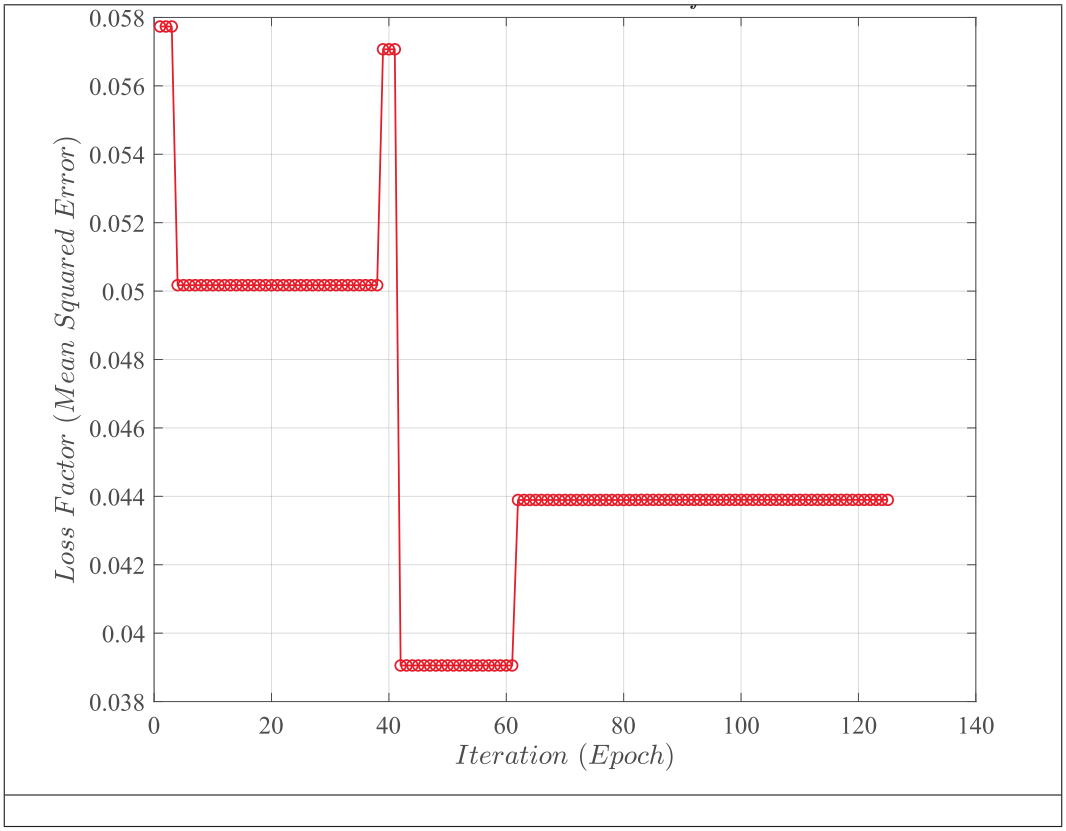

Fig. 18. Loss factor, measured as the Mean Squared Error, plotted against the number of iterations for an HDNNM.

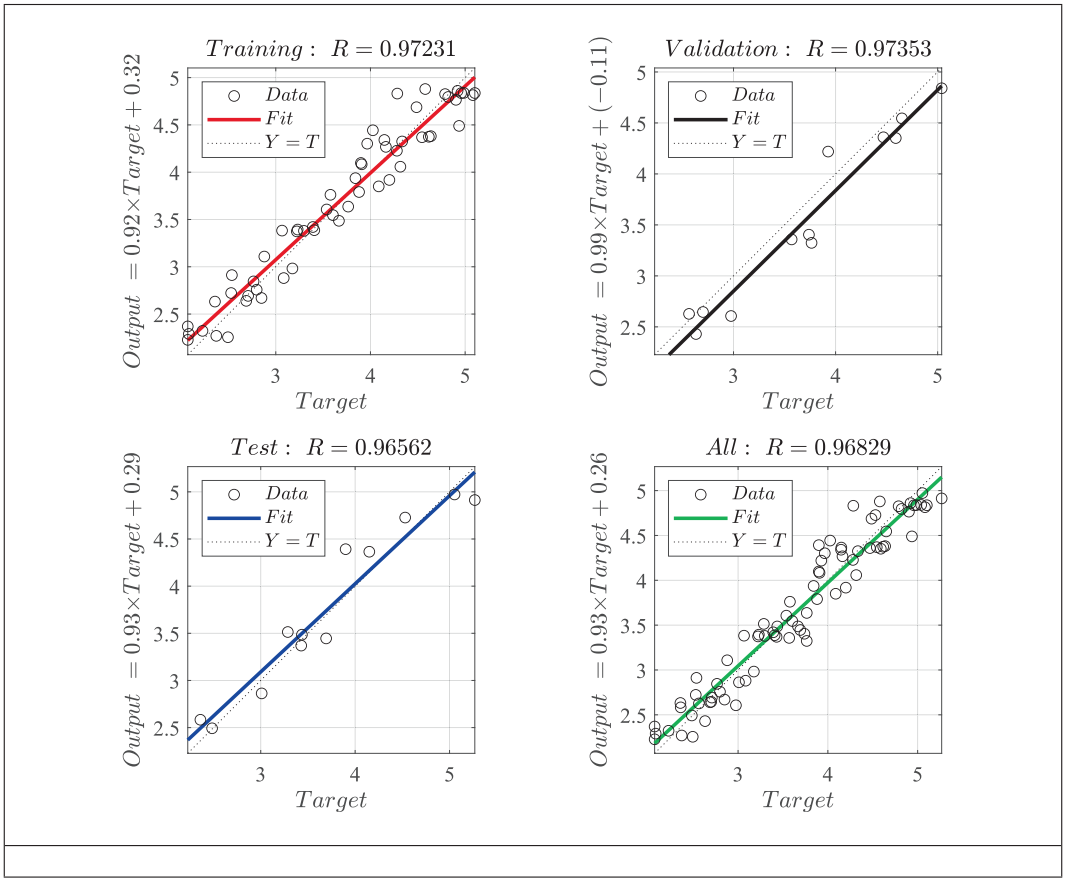

Fig. 19. Various output and target points of the mentioned hybrid DNN.

applications to manage noise and enhance system efficiency.

Fig. 13 shows the nonlinear phase velocity as a function of airflow velocity for varying graphene platelet layer weight fractions, ranging from 0 % to 1.5 %. The curves reveal that as the GPL weight fraction increases, the NPV at a given airflow velocity also increases. Specifically, at lower airflow velocities, the NPV values are higher for greater GPL content, indicating that the inclusion of GPLs enhances the wave propagation speed. The effect of GPLs is particularly noticeable at moderate airflow velocities, where the material's influence on the acoustic wave properties is most pronounced. As the airflow velocity increases, the NPV approaches similar values across different GPL concentrations, suggesting that the effect of GPLs becomes less significant at higher flow velocities. This behavior demonstrates the strong dependence of nonlinear phase velocity on the material properties, such as the GPL content, particularly at lower to moderate airspeeds, where the material's structure plays a more dominant role in wave dynamics.

Fig. 14 illustrates the relationship between nonlinear phase velocity and the GPLs' weight fraction for different wave numbers at two different values of air velocity ratio. On the left panel, where $V_{air}/V_0 = 1.5$, the graph depicts how the NPV increases with g_{GPL} for increasing values of K_x. The curves for$K_x = 50$, 100, 150, and 200 show distinct trends: as g_{GPL} rises, the NPV tends to increase, with the higher K_x values showing steeper slopes. On the right panel, for $V_{air}/V_0 = 3$, a similar pattern is observed, but the NPV values are generally higher across the board compared to the left panel. The curves for each K_x maintain their trend, but with a noticeable increase in values due to the higher air velocity ratio, signifying a stronger dependence of NPV on air flow velocity and GPLs' weight fraction. These results highlight the influence of both the excitation frequency and air flow on the dynamic response of the system, particularly for different wave numbers.

Fig. 15 depicts the nonlinear phase velocity as a function of the GPL weight fraction for different airflow velocities. The curves show how the NPV increases with the GPL weight fraction for all airflow velocities. At lower GPL concentrations, the NPV is relatively low, but as the GPL content increases, the phase velocity also increases. The effect of airflow velocity on the NPV is also evident: at higher airspeeds, the NPV reaches higher values even for low GPL content. The trend suggests that the presence of GPLs enhances the propagation of acoustic waves, particularly at higher airspeeds, where the material's influence on wave propagation becomes more pronounced. This result is significant for optimizing the material properties of solar cells or other acoustic structures, as increasing GPL concentration can improve the efficiency of sound wave transmission or damping, depending on the specific application. The figure emphasizes the nonlinear interactions between material composition (specifically the GPL content) and airflow velocity, highlighting how these factors jointly affect the system's overall acoustic performance.

Fig. 16 presents the frequency-wave number dispersion plots for symmetric and antisymmetric modes of Lamb waves, in both logarithmic and linear scales, at a fixed GPL weight fraction. The top-left panel shows the symmetric modes in a log scale, where the wave number increases with frequency, and a pronounced wave propagation pattern emerges. The intensity of the waves is depicted using a color gradient, with red indicating higher intensities and blue indicating lower intensities. The corresponding antisymmetric mode plot in the bottom-left panel follows a similar trend, but with a distinct pattern showing the behavior of antisymmetric waves. In the right panels, the same modes are displayed using a linear scale, providing a clearer, less compressed view of the dispersion relations. The symmetric modes are shown in blue, with the intensity color scale showing minimal variation in comparison to the logarithmic scale, while the antisymmetric modes display similar results, but with a slightly different wave propagation

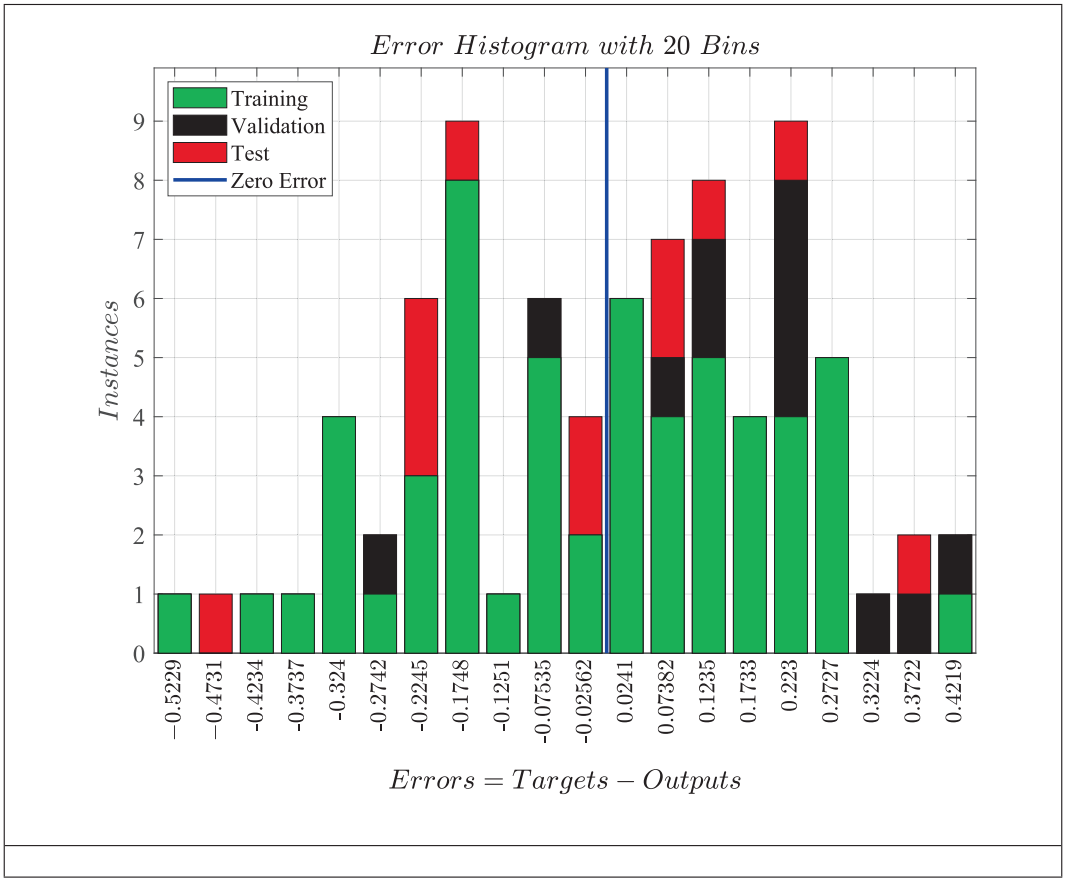

Fig. 20. Error instances across different phases of a hybrid deep neural network model's training, validation, and testing processes.

characteristic. This figure provides essential insights into the wave dynamics and dispersion characteristics for both mode types in the presence of nonlinearities.

Fig. 17 presents the 3D dispersion plots for the symmetric and antisymmetric modes of Lamb waves, displayed in both logarithmic and linear scales. The figure is divided into four panels, with the top-left and bottom-left showing the symmetric and antisymmetric modes in logarithmic scale, respectively, while the top-right and bottom-right display the same modes in linear scale. The symmetric modes (top panels) exhibit a significant variation in amplitude with respect to both frequency and wave number, with the log scale plot (top-left) highlighting the steep increase in amplitude as the wave number approaches zero, reaching a peak at lower frequencies before leveling off. In the linear scale (top-right), this trend is less pronounced, and the overall amplitude pattern appears smoother, emphasizing the nature of wave propagation for symmetric modes in linear terms. The antisymmetric modes, shown in the bottom panels, exhibit similar characteristics but with a different pattern in the distribution of amplitude. The log scale plot (bottom-left) demonstrates a sharp peak in amplitude for lower frequencies and wave numbers, whereas the linear scale plot (bottom-right) reveals a smoother transition, indicating the wave characteristics across a broader spectrum. This figure effectively compares the behavior of symmetric and antisymmetric modes, offering insights into how different scales impact the representation of Lamb wave dynamics.

5.3. Outcomes of hybrid deep neural networks (HDNNs)

In recent advancements of machine learning for predicting vibrational features of the presented green structure, a hybrid deep neural network model, referred to as HydroDL, integrates CNNs, LSTM networks, and ConvLSTM layers. This model is designed to capture and analyze complex spatial and temporal patterns inherent in the behavior of the presented green structure under various electrodynamic conditions. The CNNs excel in extracting spatial features from the structure's grid-like data, while LSTMs are adept at learning temporal dependencies over sequential time steps. The ConvLSTM layers combine these strengths by processing spatiotemporal data, allowing the model to efficiently handle and predict features affected by both spatial geometry and temporal dynamics. The integration of these neural network architectures enables HydroDL to leverage the spatial feature extraction capabilities of CNNs and the sequence learning capabilities of LSTMs, resulting in a robust predictive model. This hybrid approach provides a comprehensive framework for estimating electrodynamics features, such as frequency and amplitude variations, in the presented green structure. The model's ability to manage complex input patterns and temporal sequences makes it a powerful tool for advanced material analysis and design. Fig. 18 presents the loss factor, measured as the Mean Squared Error (MSE), plotted against the number of iterations (epochs) for an HDNNM. This model was presumably trained on a sequence-based dataset, where the objective is to minimize the loss over successive epochs. From the plot, it is evident that the loss factor exhibits a stepped pattern rather than a smooth, continuous decrease, which could indicate several key phenomena in the training process. Initially, the loss is relatively high, hovering around 0.058. However, as training progresses, the loss drops in discrete steps, reaching as low as approximately 0.038. The presence of plateaus, where the loss remains constant over several iterations, suggests that the model might be getting stuck in local minima or encountering regions of the loss landscape where gradients are small. This behavior is not uncommon in deep learning models, particularly in hybrid architectures where different layers (e.g., CNNs, LSTMs) might adapt at different rates due to their varying characteristics. The sharp drops in loss indicate that at specific points, the

Table 3
Key hyperparameters for training the hybrid deep neural network model in analyzing nonlinear aeroacoustic characteristics of solar cell structures.

Hyperparameter	Description	Value
Learning Rate	Controls the step size during optimization	0.01
Batch Size	Number of training examples used in one iteration	64
Epochs	Number of complete passes through the entire training dataset	500
Optimizer	Algorithm used for minimizing the loss function	Adam
Loss Function	Metric used to compute model error	Mean Squared Error (MSE)
Dropout Rate	A fraction of neurons dropped during training to prevent overfitting	0.5
Hidden Layers (CNN)	Number of convolutional layers in the CNN part	4 layers
Filters (CNN)	Number of filters in each convolutional layer	64
Kernel Size (CNN)	Size of convolutional kernels	(5, 5)
LSTM Units	Number of units in the LSTM layer	200
LSTM Dropout	Dropout applied to LSTM units	0.4
ConvLSTM Units	Number of units in ConvLSTM layer	128
ConvLSTM Kernel Size	Size of the kernel in the ConvLSTM layer	(5, 5)
Regularization (L2)	L2 regularization strength	0.1
Weight Initialization	Method used to initialize the network weights	Glorot Normal
Activation Function	Function applied to neurons in hidden layers	ReLU
Validation Split	Percentage of the data reserved for validation	0.3
Loss Factor (α)	Scaling factor applied to balance loss components	1.0
MSE	A metric to measure the model's prediction error	0.045
R^2 (Coefficient of Determination)	A metric to measure the model's fit to the data	0.96829
Training Data Size	Total number of training samples used	10,000 samples
Parameter Range Covered	Range of parameters covered in training data	GPL weight fraction (0.1–0.3), Airflow velocity ratio (0–0.6)
Preprocessing Methods	Techniques used to normalize or preprocess the training data	Min-max normalization applied to input parameters

model parameters undergo significant adjustments, possibly due to learning rate changes, optimization momentum, or the model overcoming a local minimum. The final steady state of the loss factor implies that the model has converged, though the stepwise nature of the decline hints at the complex dynamics within the hybrid DNN, where different components of the model may be contributing unevenly to the overall learning process.

Fig. 19 consists of four scatter plots, each representing the relationship between the predicted output of a model and the actual target values. Each subplot also includes a linear fit line and an equation describing the relationship between the output and target, as well as a diagonal reference line where $Y = T$, which represents a perfect prediction scenario.

5.3.1. Explanation of each subplot

5.3.1.1. Top left (Red fit Line).

- Equation:$Output = 0.92 \times Target + 0.32$
- The slope of 0.92 suggests that the model's predictions are slightly underestimating the target values, as the slope is less than 1. The positive intercept of 0.32 further indicates a slight bias towards higher predictions when the target values are low.

5.3.1.2. Top right (Black fit Line).

- Equation:$Output = 0.99 \times Target + (-0.11)$
- This plot shows a near-perfect slope of 0.99, which is very close to 1, indicating that the model's predictions align almost linearly with the target values. The small negative intercept suggests a minimal downward adjustment in predictions across the range of target values.

5.3.1.3. Bottom left (Blue fit Line).

- Equation:$Output = 0.93 \times Target + 0.29$
- Similar to the top left plot, this plot has a slope of 0.93, indicating a slight underestimation of target values by the model. The positive intercept of 0.29 suggests that predictions are biased slightly upward, especially at lower target values.

5.3.1.4. Bottom right (Green fit Line).

- Equation: O $utput = 0.93 \times Target + 0.26$
- This subplot is similar to the bottom left, with a slope of 0.93 and a positive intercept of 0.26. This indicates a consistent underestimation by the model across the range, with a small upward bias in predictions.

5.3.2. General Interpretation

5.3.2.1. Accuracy and bias. The slopes across all subplots are close to 1 but slightly less, suggesting that the model's predictions are generally accurate but tend to slightly underestimate the actual values. The positive intercepts in most plots indicate a small, consistent bias in the predictions.

5.3.2.2. Fit line. The closeness of the fit lines to the diagonal $Y = T$ line reflects the degree of accuracy of the model. The black fit line (top right) is the closest to $Y = T$, indicating that the model corresponding to this plot performs best in terms of minimizing both bias and variance.

5.3.2.3. Scatter distribution. The scatter of points around the fit lines provides a visual indication of the prediction errors. A tighter cluster of points around the fit line suggests lower prediction error, while more scattered points indicate higher error. In summary, the figure demonstrates that the model predictions are reasonably close to the actual targets but with a tendency to slightly underestimate the target values, as indicated by the slopes slightly less than 1 and the consistent positive intercepts.

Fig. 20 represents the distribution of error instances across different phases of a DNN model's training, validation, and testing processes. The bar chart is segmented into three categories: Training (green bars), Validation (black bars), and Test (red bars), which reflect the number of instances where the network encounters errors during each respective phase. The height of each bar indicates the frequency of errors, with the green bars representing training errors, black bars representing validation errors, and red bars representing test errors. The blue vertical line labeled as "Zero Error" serves as a reference for an ideal scenario where no errors occur across all phases. The figure shows that the model experiences varying levels of errors, with some instances showing zero

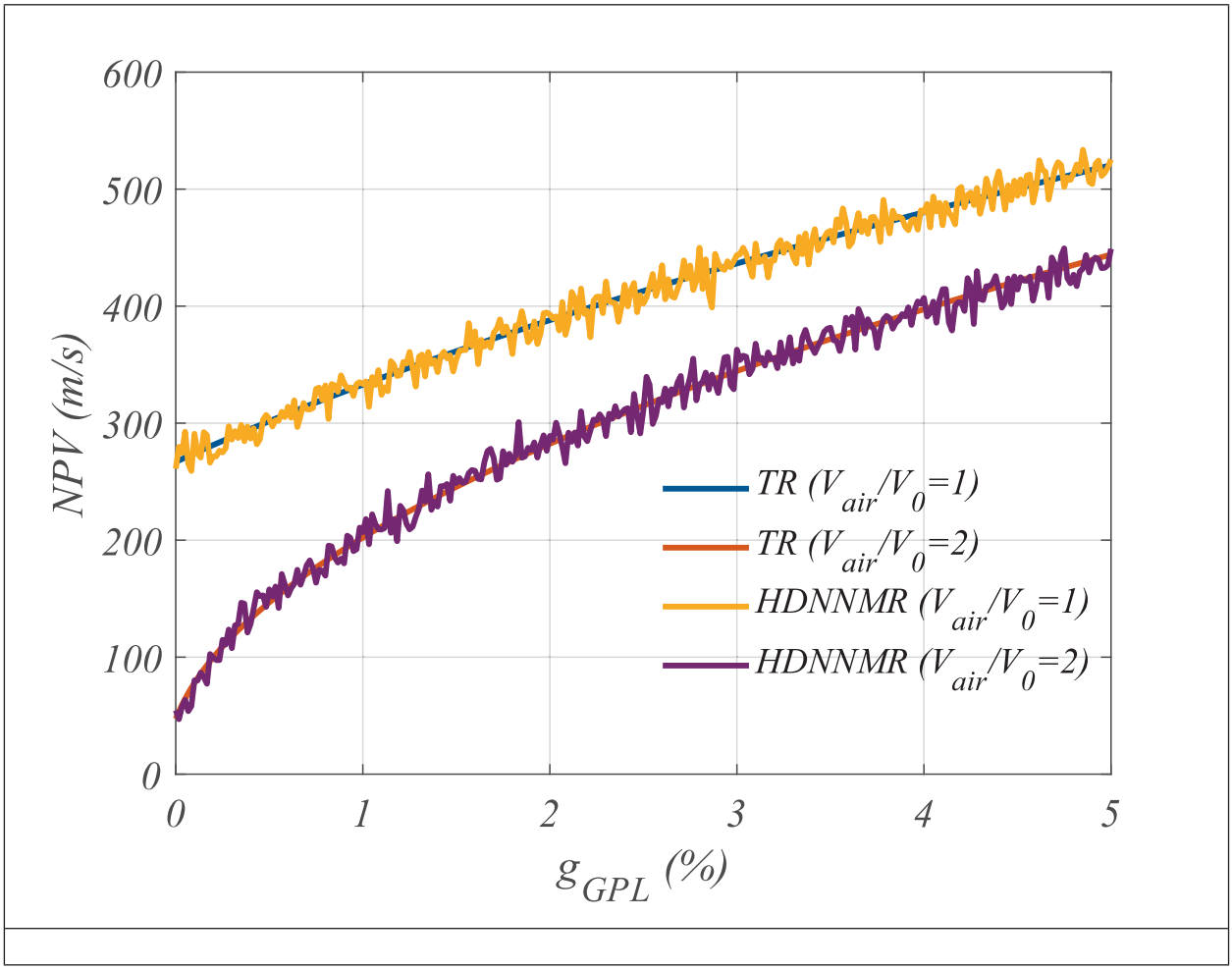

Fig. 21. A comparison between theoretical results and hybrid deep neural network model results for NPV as a function of the GPLs' weight fraction.

errors in the test and validation phases, indicating good performance. However, the presence of bars in all three colors, particularly in the validation and test phases, suggests that the model has not completely generalized to unseen data. This error analysis provides insight into the model's overfitting or underfitting tendencies and helps in diagnosing areas where the model's architecture or training process might need improvement.

Table 3 summarizes key hyperparameters for training the hybrid deep neural network model in analyzing nonlinear aeroacoustic characteristics of solar cell structures. Key parameters include learning rate, batch size, epochs, and optimizers, with values tailored for effective convergence. The CNN, LSTM, and ConvLSTM layers are configured with varying numbers of filters, units, and kernel sizes to capture spatial and temporal dynamics. Regularization techniques, such as dropout and L2 regularization, are applied to prevent overfitting. Performance metrics like RMSE and R^2 are used to evaluate model accuracy, with a loss factor balancing error components.

Fig. 21 presents a comparison between theoretical results (TR) and hybrid deep neural network model results for NPV as a function of the GPLs' weight fraction. Four distinct scenarios are examined, corresponding to different ratios of air velocity to reference velocity. The blue and orange curves represent the theoretical results for $V_{air}/V_0 = 1$ and $V_{air}/V_0 = 2$, respectively, while the yellow and purple curves illustrate the corresponding HDNNMR results under the same velocity ratios. Both TR and HDNNMR exhibit an increasing NPV with rising g_{GPL}, but HDNNMR consistently predicts higher NPV values. The discrepancy between the theoretical and hybrid model results becomes more pronounced as g_{GPL} increases, demonstrating HDNNMR's greater sensitivity to changes in g_{GPL}. This suggests that the hybrid deep neural network model is more capable of capturing the nonlinear dynamics of the system, offering more precise predictions compared to traditional theoretical methods.

6. Conclusion

This study has introduced a novel metrological framework for analyzing the nonlinear phase velocity, lamb wave propagation, and aeroacoustic behavior of multi-layer silicon solar cell structures reinforced with GPL-metal layers. By incorporating advanced theories such as HSDT and MCST, we have developed a comprehensive model that accurately captures the mechanical and acoustic interactions in the presence of external sound radiation and airflow pressure. The application of the variational energy technique and harmonic-based methods has enabled the resolution of the governing partial differential equations, while Newmark's time integration scheme has provided precise simulations of dynamic vibrations. The validation of the framework using an HDNNM has demonstrated the effectiveness of machine learning in enhancing the accuracy of predictions for nonlinear acoustic responses and vibration characteristics. Through the integration of physical modeling with AI-based algorithms, we have achieved a robust system that can predict the effects of various parameters, such as GPL weight fraction and airflow velocity, on the dynamic behavior of solar cells. Our findings have shown that GPL reinforcement significantly improves the stiffness and damping properties of the solar cell

structures, thereby enhancing their acoustic resilience and overall energy conversion stability. The study has provided valuable insights into the role of vibro-acoustic interactions in the performance of solar cells under real-world operational conditions. Furthermore, it has highlighted the potential of the proposed framework for use in structural health monitoring and optimization of next-generation solar energy devices. Overall, the methodology presented in this research has offered new perspectives on the metrological assessment of solar cell structures, marking a significant advancement in the fields of acoustic measurement, materials science, and energy technology. It has laid the groundwork for further exploration of the complex interactions between materials and dynamic loading conditions in solar energy systems, opening up new avenues for enhancing their efficiency, durability, and environmental resilience.

CRediT authorship contribution statement

Qiang Zhang: Visualization, Validation, Data curation, Conceptualization, Investigation, Methodology, Resources, Software, Writing – original draft, Writing – review & editing. **Lei Chang:** Writing – original draft, Validation, Data curation, Conceptualization, Software, Supervision, Visualization, Writing – review & editing. **Mohammed El-Meligy:** Visualization, Software, Data curation, Conceptualization, Resources, Validation, Writing – review & editing. **Khalid A. Alnowibet:** Investigation, Methodology, Resources, Validation, Writing – review & editing.

Declaration of competing interest

The authors declare that they have no known competing financial interests or personal relationships that could have appeared to influence the work reported in this paper.

Acknowledgment

The authors extend their appreciation to King Saud University, Saudi Arabia for funding this work through Ongoing Research Funding Program, (ORF-2025-305), King Saud University, Riyadh, Saudi Arabia.

Data availability

Data will be made available on request.

References

[1] J. Perlin, From space to earth: the story of solar electricity, Earthscan (1999).
[2] C.M. Green, M. Lomask, Vanguard: A history, 1970.
[3] H. Yoon, J.E. Granata, P. Hebert, R.R. King, C.M. Fetzer, P.C. Colter, K. M. Edmondson, D. Law, G.S. Kinsey, D.D. Krut, Recent advances in high-efficiency III–V multi-junction solar cells for space applications: ultra triple junction qualification, Prog. Photovolt. Res. Appl. 13 (2005) 133–139.
[4] A. Luque, S. Hegedus, Handbook of photovoltaic science and engineering, John Wiley & Sons, 2011.
[5] N.S. Lewis, Research opportunities to advance solar energy utilization, Science 351 (2016) aad1920.
[6] M.A. Green, A. Ho-Baillie, H.J. Snaith, The emergence of perovskite solar cells, Nat. Photonics 8 (2014) 506–514.
[7] M. Woodhouse, R. Jones-Albertus, D. Feldman, R. Fu, K. Horowitz, D. Chung, D. Jordan, S. Kurtz, On the path to sunshot. The role of advancements in solar photovoltaic efficiency, reliability, and costs, National Renewable Energy Lab. (NREL), Golden, CO (United States), 2016.
[8] N.-G. Park, M. Grätzel, T. Miyasaka, K. Zhu, K. Emery, Towards stable and commercially available perovskite solar cells, Nat. Energy 1 (2016) 1–8.
[9] I. Cardinaletti, T. Vangerven, S. Nagels, R. Cornelissen, D. Schreurs, J. Hruby, J. Vodnik, D. Devisscher, J. Kesters, J. D'Haen, Organic and perovskite solar cells for space applications, Sol. Energy Mater. Sol. Cells 182 (2018) 121–127.
[10] P. Pal, S.K. Das, D. Dey, K. Chakrabarti, Photovoltaic integrated solar induction heater using voltage source inverter, ES Energy Environ. 16 (2022) 26–29.
[11] T. Zhao, M.J. Bayat, K. Asemi, Free vibration analysis of functionally graded multilayer hybrid composite cylindrical shell panel reinforced by GPLs and CNTs surrounded by Winkler elastic foundation, Eng. Struct. 308 (2024) 117975.
[12] A. Kalhori, M.J. Bayat, K. Asemi, Buckling analysis of stiffened functionally graded multilayer graphene platelet reinforced composite plate with circular cutout embedded on elastic support subjected to in-plane normal and shear loads, Results Eng. 20 (2023) 101563.
[13] M. Babaei, F. Kiarasi, K. Asemi, Torsional buckling response of FG porous thick truncated conical shell panels reinforced by GPLs supporting on Winkler elastic foundation, Mech. Based Des. Struct. Mach. 52 (2024) 3552–3581.
[14] G.R. Asgari, A. Arabali, M. Babaei, K. Asemi, Dynamic instability of sandwich beams made of isotropic core and functionally graded graphene platelets-reinforced composite face sheets, Int. J. Struct. Stab. Dyn. 22 (2022) 2250092.
[15] M.R. Barati, A.M. Zenkour, Analysis of postbuckling of graded porous GPL-reinforced beams with geometrical imperfection, Mech. Adv. Mater. Struct. 26 (2019) 503–511.
[16] N. Ghavidel, A. Alibeigloo, Free vibration analysis of cylindrical sandwich panel with electro-rheological core and FG-GPLRC facing sheets based on First order shear deformation theory referred by Qatu, J. Vibrat. Control (2023) 10775463221148535.
[17] C. Feng, S. Kitipornchai, J. Yang, Nonlinear free vibration of functionally graded polymer composite beams reinforced with graphene nanoplatelets (GPLs), Engineering Structures 140 (2017) 110–119.
[18] Z. Zhou, Y. Wang, S. Zhang, R. Dimitri, F. Tornabene, K. Asemi, Numerical study on the buckling behavior of FG porous spherical caps reinforced by graphene platelets, Nanomaterials 13 (2023) 1205.
[19] X. Huang, W. Mo, W. Sun, W. Xiao, Buckling analysis of porous functionally graded GPL-reinforced conical shells subjected to combined forces, Arch. Appl. Mech. 94 (2024) 299–313.
[20] Z. Feng, X. Yang, H. Keshavarzpour, A. Ghasemi, Free vibration analysis of hybrid CNT/GPL-reinforced Porous composite plates under fluid-loading, Aerosp. Sci. Technol. 148 (2024) 109116.
[21] C. Feng, S. Kitipornchai, J. Yang, Nonlinear bending of polymer nanocomposite beams reinforced with non-uniformly distributed graphene platelets (GPLs), Compos. B Eng. 110 (2017) 132–140.
[22] Y. Wang, C. Feng, C. Santiuste, Z. Zhao, J. Yang, Buckling and postbuckling of dielectric composite beam reinforced with Graphene Platelets (GPLs), Aerosp. Sci. Technol. 91 (2019) 208–218.
[23] H.-X. Ding, M. Eltaher, G.-L. She, Nonlinear low-velocity impact of graphene platelets reinforced metal foams cylindrical shell: effect of spinning motion and initial geometric imperfections, Aerosp. Sci. Technol. 140 (2023) 108435.
[24] H. Fourn, H.A. Atmane, M. Bourada, A.A. Bousahla, A. Tounsi, S.R. Mahmoud, A novel four variable refined plate theory for wave propagation in functionally graded material plates, Steel Compos. Struct. Int. J. 27 (2018) 109–122.
[25] T.Q. Quan, N. Dinh Duc, Nonlinear vibration and dynamic response of shear deformable imperfect functionally graded double-curved shallow shells resting on elastic foundations in thermal environments, J. Therm. Stresses 39 (2016) 437–459.
[26] A. Eyvazian, C. Zhang, Ö. Civalek, A. Khan, T.A. Sebaey, N. Farouk, Wave propagation analysis of sandwich FGM nanoplate surrounded by viscoelastic foundation, Arch. Civ. Mech. Eng. 22 (2022) 159.
[27] F. Ebrahimi, M.R. Barati, P. Haghi, Thermal effects on wave propagation characteristics of rotating strain gradient temperature-dependent functionally graded nanoscale beams, J. Therm. Stresses 40 (2017) 535–547.
[28] F. Ebrahimi, M.R. Barati, A. Dabbagh, A nonlocal strain gradient theory for wave propagation analysis in temperature-dependent inhomogeneous nanoplates, Int. J. Eng. Sci. 107 (2016) 169–182.
[29] W. Yang, L. Chang, K.A. Alnowibet, M. El-Meligy, Enhancing the efficiency and energy capacity of the tri-directional FG nanoplate attached to the piezoelectric patch validated by artificial intelligence, Aerosp. Sci. Technol. 155 (2024) 109694.
[30] R. Moradi-Dastjerdi, K. Behdinan, Stress waves in thick porous graphene-reinforced cylinders under thermal gradient environments, Aerosp. Sci. Technol. 110 (2021) 106476.
[31] L. Chang, K.A. Alnowibet, Application of machine learning algorithm to measure nonlinear transient frequencies of the centrifugal systems under moving loads with velocity acceleration, Measurement 227 (2024) 114271.
[32] N. Chen, P. Yan, J. Ouyang, An improved model analysis approach for hybrid thermo-piezoelectric micro actuator with thermo-piezoelectric coupling, Measurement 136 (2019) 517–524.
[33] G. Sha, W. Xiao, H. Zuo, M. Cao, M. Radzieński, W. Ostachowicz, Global-local damage localization and imaging in beam structures using laser-measured natural frequencies and guided wavefields, Measurement 115061 (2024).
[34] J.-M. Hyun, J.-R. Lee, Evaluation of electromagnetic characteristics of 3D-printed radar absorbing structures based on three-dimensional period pattern surface, Measurement 227 (2024) 114213.
[35] M. Kulpa, T. Howiacki, A. Wiater, T. Siwowski, R. Sieńko, Strain and displacement measurement based on distributed fibre optic sensing (DFOS) system integrated with FRP composite sandwich panel, Measurement 175 (2021) 109099.
[36] J. Liu, G. Cao, H. Wang, C. Cui, Z. Liu, Development of intelligent methodologies perceiving microstructure and mechanical properties of hot rolled steels, Measurement 221 (2023) 113526.
[37] W. Gao, Z. Qin, F. Chu, Wave propagation in functionally graded porous plates reinforced with graphene platelets, Aerosp. Sci. Technol. 102 (2020) 105860, https://doi.org/10.1016/j.ast.2020.105860.
[38] Y. Wang, C. Feng, C. Santiuste, Z. Zhao, J. Yang, Buckling and postbuckling of dielectric composite beam reinforced with Graphene Platelets (GPLs), Aerosp. Sci. Technol. 91 (2019) 208–218, https://doi.org/10.1016/j.ast.2019.05.008.
[39] R. Muni Rami Reddy, W. Karunasena, W. Lokuge, Free vibration of functionally graded-GPL reinforced composite plates with different boundary conditions, Aerospace Sci. Technol. 78 (2018) 147–156. https://doi.org/10.1016/j.ast.2018.04.019.

[40] F.L. Yang, Y.Q. Wang, Y. Liu, Low-velocity impact response of axially moving functionally graded graphene platelet reinforced metal foam plates, Aerosp. Sci. Technol. 123 (2022) 107496, https://doi.org/10.1016/j.ast.2022.107496.
[41] Y. Wang, R. Zeng, M. Safarpour, Vibration analysis of FG-GPLRC annular plate in a thermal environment, Mech. Based Des. Struct. Mach. 50 (2022) 352–370, https://doi.org/10.1080/15397734.2020.1719508.
[42] B. Yang, S. Kitipornchai, Y.-F. Yang, J. Yang, 3D thermo-mechanical bending solution of functionally graded graphene reinforced circular and annular plates, App. Math. Model. 49 (2017) 69–86, https://doi.org/10.1016/j.apm.2017.04.044.
[43] B. Karami, D. Shahsavari, On the forced resonant vibration analysis of functionally graded polymer composite doubly-curved nanoshells reinforced with graphene-nanoplatelets, Comput. Methods Appl. Mech. Eng. 359 (2020) 112767.
[44] F. Cornacchia, N. Fantuzzi, R. Luciano, R. Penna, Solution for cross- and angle-ply laminated Kirchhoff nano plates in bending using strain gradient theory, Compos. B Eng. 173 (2019) 107006, https://doi.org/10.1016/j.compositesb.2019.107006.
[45] J.N. Reddy, An Introduction to Nonlinear Finite Element Analysis Second Edition: with applications to heat transfer, fluid mechanics, and solid mechanics, OUP Oxford, 2014.
[46] F. Abad, J. Rouzegar, Exact wave propagation analysis of moderately thick Levy-type plate with piezoelectric layers using spectral element method, Thin-Walled Struct. 141 (2019) 319–331.
[47] F. Abbaspour, H. Arvin, M. Shahriari-kahkeshi, Nonlinear vibration control of a piezoelectric graphene sheet reinforced microplate with thermal uncertainty: Feedback linearization and sliding mode approaches, Thin-Walled Struct. 181 (2022) 110129.
[48] N.V. Nguyen, K.Q. Tran, D.T.T. Do, C.H. Thai, K.K. Żur, H. Nguyen-Xuan, An isogeometric analysis of solar panels with a bio-inspired substrate, Eng. Anal. Bound. Elem. 166 (2024) 105854, https://doi.org/10.1016/j.enganabound.2024.105854.
[49] S.I. Tahir, A. Tounsi, A. Chikh, M.A. Al-Osta, S.U. Al-Dulaijan, M.M. Al-Zahrani, An integral four-variable hyperbolic HSDT for the wave propagation investigation of a ceramic-metal FGM plate with various porosity distributions resting on a viscoelastic foundation, Waves Random Complex Media (2021) 1–24, https://doi.org/10.1080/17455030.2021.1942310.
[50] H. Aminipour, M. Janghorban, Wave propagation in anisotropic plates using trigonometric shear deformation theory, Mech. Adv. Mater. Struct. 24 (2017) 1135–1144, https://doi.org/10.1080/15376494.2016.1227500.
[51] M.R. Nami, M. Janghorban, Wave propagation in rectangular nanoplates based on strain gradient theory with one gradient parameter with considering initial stress, Mod. Phys. Lett. B 28 (2014) 1450021.